# LuxAct: Enhance Everyday Objects with Interaction-Powered Illumination for Visual Communication

Xiaoying Yang
University of California, Los Angeles
Los Angeles, California, USA
xiaoyingy@ucla.edu

Qian Lu
Texas A&M University
College Station, Texas, USA
qianlu@tamu.edu

Jeeeun Kim
Texas A&M University
College Station, Texas, USA
jeeeun.kim@tamu.edu

Yang Zhang
University of California, Los Angeles
Los Angeles, California, USA
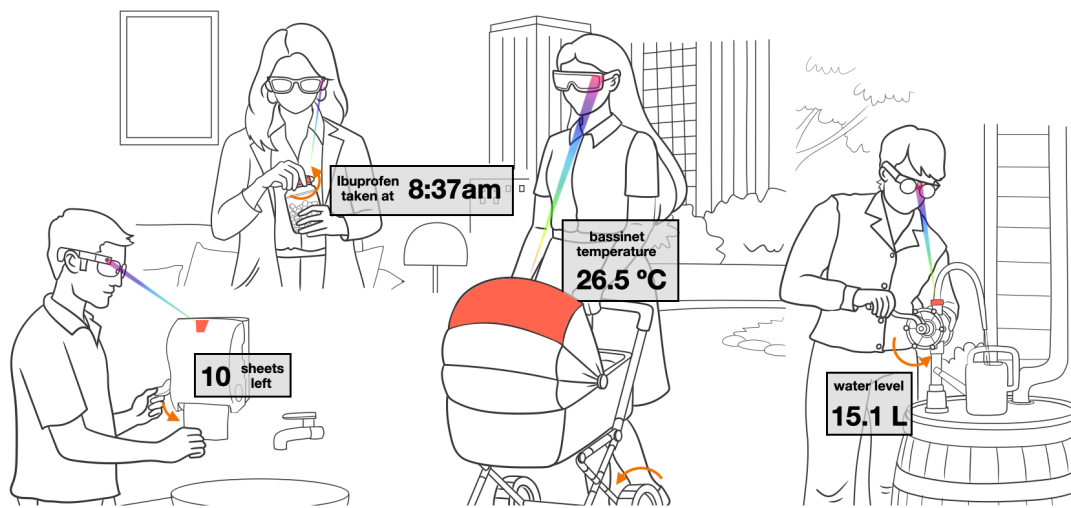yangzhang@ucla.edu

Figure 1: We envision LuxAct being integrated into everyday objects such as pill bottle, paper towel dispenser, baby stroller, and rain-collecting barrel, imbuing sensing and interactivity to improve context awareness and enrich AR experiences.

## ABSTRACT

Imbuing sensing and interactivity into everyday objects has long been sought after within the HCI community to facilitate richer and more immersive user experiences. However, conventional methods rely on costly hardware, such as embedded sensor tags, or passive visual markers that lack digital capabilities to sense user context. We present *LuxAct*, an interaction-powered visual communication system that enables everyday objects to encode their information and user interaction data into sequences of RGB color light. These sequences are decoded by Point of View (POV) cameras on AR headsets or smart glasses to derive meaningful information from interactions. *LuxAct* are self-powered and ultra-low-cost, leveraging striking and plucking on piezoelectric generators to harvest energy from user interactions. Through strategic pattern design, our system transforms visual channels into carriers of both object identification and sensory data, supporting applications with rich sensing needs. We demonstrated a wide range of use cases, including interactive controls, sensate storage, smart water hose, medicine reminder, fingertip probes and beyond, offering a practical alternative for digitalizing passive objects to enable ubiquitous sensing in AR-enhanced environments.

## CCS CONCEPTS

• **Hardware** → **Sensor applications and deployments**; • **Human-centered computing** → **Human computer interaction (HCI)**.

## KEYWORDS

Interaction Power; Battery-Free; Ubiquitous Computing; Visible Light Communication; Augmented Reality

**ACM Reference Format:**
Xiaoying Yang, Qian Lu, Jeeeun Kim, and Yang Zhang. 2025. LuxAct: Enhance Everyday Objects with Interaction-Powered Illumination for Visual Communication. In *The 38th Annual ACM Symposium on User Interface*

## 1 INTRODUCTION

Sensing user interactions forms the backbone of a wide array of HCI applications, from smart homes to wearables like smart glasses, with rising interest in advancing these capabilities for richer AR interactions. However, scaling such capabilities faces significant challenges. On the AR device side, adding sophisticated sensors to wearables is limited by stringent constraints on power, size, and form factor. On the object side, incorporating digital components into passive objects and environments requires significant mental and physical effort to maintain the power of these thousands of objects in various locations. Consequently, current practice in physical-digital integration is still confined to two extremes: low-cost, passive markers such as QR codes and RFID tags for object identification, or expensive, powered digital devices such as smart home sensors for sensing, as illustrated at the two ends of Figure 2.

In response, extensive research in the HCI community has been motivated toward ultra-low-cost, low-power, or passive interfaces for interactive sensing. For example, self-powered sensors are designed to convert a broad range of user activities into electrical signals, which, however, rely on costly and custom-built hardware to retrieve the data and are poorly suited for integration into AR wearables [5, 6, 34, 76, 82, 86]. Passive interfaces are created to strategically convert static information, such as object identification (ID), and dynamic user inputs, such as pressing buttons and sliding knobs, into acoustic signals captured by microphones [24, 41, 62] or optical signal changes perceived by camera sensors [10, 17, 18, 49, 84, 87].

In this research, we extend the potential of interactive sensing through visual channels. We propose *LuxAct*, the design of interaction-powered illumination mechanisms that enhance everyday objects with visual communication capabilities through sequential color patterns. We identify visible light as a promising carrier signal to encode user activity and interaction information, for the benefits it offers: First, light emitters (i.e., LEDs) often feature their light-weight nature, broad viewing angle, low power consumption, and affordability [51]. They effectively address concerns regarding scalability and power efficiency in augmenting passive daily objects with digital capabilities. Second, the broad color space in the light wavelength offers a wide spectrum for mapping sensory information for efficient data transmission [30]. This promise of light as a signal is evidenced by recent research in Visible Light Communication (VLC), using light as a communication medium in addition to illumination, in response to the growing congestion in the RF spectrum and the need for costly RF transceivers and demodulators [7, 42]. Finally, visible light as a carrier signal can be cheaply encoded with resistance, one of the most profound electrical properties. Resistances have been utilized to reflect many target signals such as force, temperature, strain, deformation, and light, enabling the conversion of a wide variety of user activities and environmental information into light variations through low-cost circuits and structurally simple mechanisms.

Closer to our research is literature which created passive visual markers for object tracking [17, 18] and tangible interfaces for interactive sensing [10, 84, 87]. However, these approaches are either
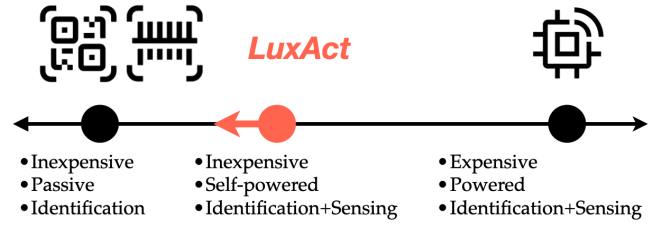


**Figure 2: On the spectrum of passive markers for identification only, and digital devices for sensing and communication, *LuxAct* is in between.**

limited by the signals they can communicate to cameras or require a large surface area to encode data. *LuxAct* showcases a broader self-powered communication capability by embedding the identification of objects, sensing of user activity and interaction, and sensing of environmental facets (e.g., resource availability, temperature), into a compact, dot-sized LED marker that communicates with RGB POV cameras. Figure 1 illustrates this vision. Specifically, our system harnesses the kinetic energy from user interactions to power multi-color LEDs, which are sequentially illuminated by a structured piezoelectric power generator. The data, comprising identification and information sensed from the environment, is modulated into colors and embedded in the geometry of the power generator, enabling the simultaneous energy conversion, sensing of interactions, and transmission of data. This system design eliminates the need for batteries, components like oscillators and micro-controllers to modulate signals for VLC, further reducing system complexity and costs, and shifting ubiquitous sensing towards the left end of the spectrum, as shown in Figure 2, to enable scalable deployment akin to passive markers to enhance AR interactivity.

To the best of our knowledge, *LuxAct* is the first research to utilize kinetic interaction energy through piezoelectric power generation to augment everyday objects with visual communication capabilities. Rather than focusing on high-fidelity sensing or superior system performance, our work emphasizes the demonstration of a complete, interaction-powered VLC system on everyday objects, supported by proof-of-concept designs, validation studies, and evaluations. Along the way, our research has revealed several limitations, including challenges in camera-LED detection under ambient lighting and body motion in AR settings, potential intrusiveness of LED signals, and the need for systematic investigation into signal modulation, which require further improvements in future work. Our research contribution is summarized as follows:

- Exploration of power generator designs with piezoelectric energy harvesting (e.g., plucking and striking) for LED illumination with minimal mechanical and electrical overhead.
- Design of an activity-sensitive information encoding scheme, and encoder modules that account for both motion dynamics and information transmission constraints.
- Implementation of first-principle algorithms for camera-LED detection and information decoding.
- Development and evaluation of 10 applications in a wide range of scenarios, including object identification, interactive controls, fingertip sensing probes, and beyond.

## 2 RELATED WORK

### 2.1 Piezoelectric Energy Harvesting

Piezoelectric effect has been primarily used for sound, vibration, and pressure sensing. In HCI community, piezoelectric effect has been utilized to design novel interfaces for sensing surface geometry [60], food intakes [67], oral health [31], human posture [12] and touch gestures on eyeglasses [74], rings [68], garments [3], object surfaces [54, 66, 80], and knock on smartphones [73], hitchhiking the acoustic and vibration signals during an interaction. In these applications, the *piezoelectric elements* (hereafter referred to as *piezos*) operate as self-powered sensors, generating differential voltage signals that are amplified and sampled using externally powered computing devices to retrieve the original information. On the other hand, piezos are made into power generators to harvest kinetic energy and supply power to external devices, with notable applications in piezoelectric floor tiles and insoles that generate power from footsteps [53, 61]. Piezos are also employed in gathering energy from water flow [36, 52], civil structure oscillations [33], object motions [44], and human body movements, including knee motions [57], breath and elbow flex [48]. Given the limited amount of power generated by piezos, considerable engineering efforts are dedicated to optimizing the design of the energy transducer, including using oscillating mechanisms to up-convert the frequency of kinetic motions to the resonant frequency of the piezoelectric materials [56]. A technological closer work investigated the performance of piezos for flashing an LED, but relied on motorized oscillating mechanisms [13], which differ from interactive power generation in our research.

### 2.2 Interaction-Powered Object Identification and State Sensing

The convergence of the physical and digital worlds has generated increasing interest in self-powered interactive interfaces, as they enable ubiquitous computing while reducing the need for manual battery maintenance. Leveraging the distinct patterns inherent in human interaction with physical objects, interaction-powered sensing has been extensively explored. Examples include Moiré patterns, which emerge from the visual interference between two superimposed linear structures with differing spatial frequencies [84], acoustic signals generated by 3D printed objects scratched by user interactions [62], capacitance changes yielded from dynamic coupling patterns [2], and RF backscatter generated through varying reflectivity [34, 69, 77]. Similar to prior work demonstrating how the sound of tearing Velcro can function as a low-cost and passive label [41], distinctive click sounds from handheld mobile VR controllers [24] can enable robust object identification and interaction detection through simple acoustic analysis. In parallel, ambient energy sources has been explored to power interactive systems without relying on conventional batteries, including light [45, 71, 82] and motions [4, 14, 47, 76].

Close work is self-powered input interfaces, which in this context refers to a compact, standalone device capable of generating power for sensing and communicating with other devices without needing any additional sensors and electronics. This has shown success in research [5, 55, 71] and commercial products including the ZF

energy harvester [81], DFRobot self-powered wireless switch, all of which convert energy into RF signals necessitating more harvested energy to function and specialized receivers to receive signals in a specific frequency, significantly hindering their deployment. Unlike these works, *LuxAct* converts energy into visible light. While a point light has also been studied as an information indicator via various light emission and changes in light intensity over time [27], *LuxAct* makes itself apart from the prior work as an optical, dot-sized marker delivering information through color changes.

### 2.3 AR Object Interaction

Interaction-driven sensing enabled communication with physical objects in virtual environments, reshaping the landscape of tangible interaction in see-through interfaces.

Sketched Reality [37] establishes synchronized bidirectional interactions between virtual sketches and physical props, while HoloBots [32] allows remote users to manipulate local tangible tokens, based on synchronized robotic devices (i.e., swarm robot platform). Augmented Object Intelligence (AOI) [19] enables seamless integration of physical objects as interactive digital media to identify objects and retrieve contextual information on the web in real time. X-AR [9] further expands interaction bandwidth between a user and physical objects by localizing and tracking RFID-tagged objects that are out of the viewing angle of AR glasses. X-Vision [25] combines RFID sensing and depth-camera pose tracking to overlay real-time data onto tagged objects using AR headsets. These works are based on the recognition of physical objects that are already known (e.g., using Toio robotic systems), or on integrating antennas to the AR glass to identify target objects tagged with RFID. *LuxAct* differentiates from these works by being able to recognize target objects when natural interaction turns into signals by actuating information and transmitting them as light signals (e.g., struck, plucked), capturing using a native RGB camera. It enables passive objects to emit structured, time-sensitive, and precise data through low-cost communication.

### 2.4 Camera-Based Communication

As cameras are becoming increasingly pervasive with ones embedded in billions of smartphones and, soon, smart glasses, cameras serve as the primary sensors for reconstructing and interpreting critical information, such as 3D printed identical objects identification using visible surface texture [17] and non-visible texture [49], interaction patterns using passive moiré encoding, where small physical movements change visual interference patterns captured by cameras [10]. Further investigating AR camera as sensing apparatus, InfraredTags [20] embeds invisible AR markers for infrared-based 3D Printing and imaging tool interpretation, Imprinto [22] employed watermarking for human and machine perception, to allow for invisible content embeddings with off-the-shelf IR inks.

This growing integration of cameras into computing devices has sparked interest in VLC, particularly camera-based VLC, as a way to hitchhike on existing cameras as free receivers to enhance communication capabilities. Extensive research has focused on the design of transceivers [8, 42] and data modulation schemes [30, 78, 79] to enhance data transmission rates [7] and extend communication range [29, 63]. The use of rapidly emitted RGB color sequences,

imperceptible to the human eye, has been explored for enabling screen-camera communication [38, 59, 72, 83]. Battery-free VLC has also been proposed to facilitate IoT sensing with visible light markers [70], tags [50, 65], reflectors [42], and interactive devices [63]. LightAnchors [1] and InfoLED [75] are pilot works introducing VLC to AR, leveraging high-frequency blinking of existing LEDs and light bulbs in the surroundings to augment the environment and communicate with mobile phones. Recently, EchoSight [43] enables bidirectional VLC using fully featured microcontroller-based systems on both tags and readers, enhancing user efficiency and experience in AR IoT applications. Unlike these prior works that focus on improving VLC data transmission range and efficiency, *LuxAct* presents a novel VLC system design that is battery-free, low-cost and powered by user interaction, augmenting passive objects and utilizing light channels to enhance AR interactivity.

## 3 POWER GENERATOR DESIGN

The power of our system is generated through dynamic mechanical deformation of piezoelectric elements. People have predominantly leveraged two modes for generating power with piezoelectric elements—*strike* (i.e., $d_{33}$) and *pluck* (i.e., $d_{31}$), with strike being more effective in generating high voltage and pluck in high current [64]. Accordingly, our work explores the design of power generators utilizing *both* modes. We conducted studies to identify the optimal mechanical structures for power generation in our system.

### 3.1 Striking-Based Power Generation

Striking motions typically appear in interactions like button presses and finger-to-surface taps. Empirically, we found that light taps on the surface of a small, single piezo disc do not generate sufficient power to activate an LED—unless an additional capacitor stores energy from multiple taps for a single discharge, or a significantly harder tap (high input force) is applied. These motions do not align well with natural user interaction and require additional mechanisms. We leveraged springs—similar to those used in piezo-based igniters—to accumulate mechanical energy, which is then released to drive a component that strikes the surface of the piezo all at once. Specifically, we 3D printed compliant structures to create a striking effect on the piezo to improve the power generation. We used a 13×13 mm, bimorph-structured *Rigid Piezo* for striking-based power generation, as shown in Figure 3C.

To understand the effect of different forms of compliant geometry in power generation, we performed a study with a simple compliant structure (Figure 3A). Bridge thicknesses greater than 0.6 mm require excessively high pressing force, while bridges thinner than 0.4 mm are beyond our fabrication capabilities using low-cost FDM 3D printers. We decided on a bridge thickness to be 0.5 mm for the following study. We then varied the angles and lengths of bridges, and the number of bridge pairs of the compliant structure, and we measured the power generated by the different geometries. Based on our experiment, when flashing an LED with the striking mechanism, the LED acts as a load of tens of kilo-ohms to the power source, so we decided on a 47 kΩ as the load to isolate the nonlinearity of LED in the power characteristics for this study. The researcher pressed the mechanisms in each configuration to strike a piezo (Figure 3A) ten times, and used an oscilloscope to record
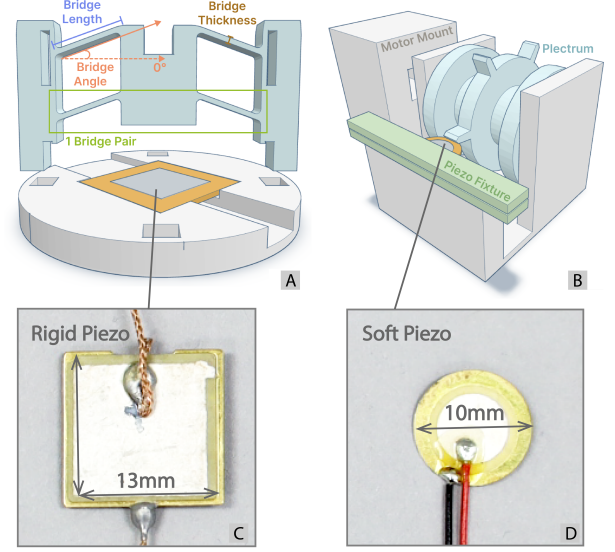


Figure 3: Modules used in validation studies of (A) striking-based and (B) plucking-based power generation. The motor mount is for the motorized plucking setup for validation studies only. (C) Rigid piezo. (D) Soft piezo.
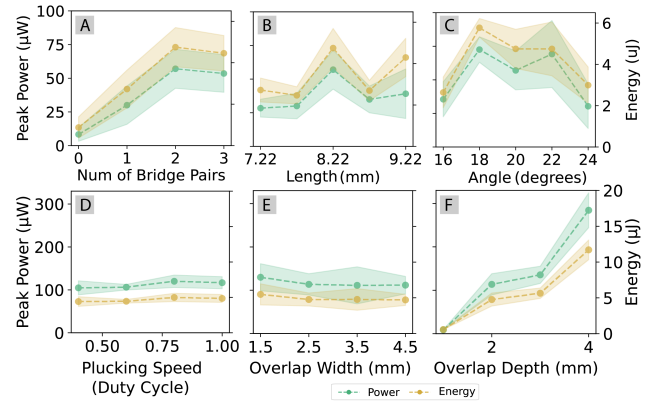


Figure 4: Variations of power and energy with different mechanics, including (A) number of bridge pairs, (B) length, and (C) angle of bridges for striking-based power generation, and (D) plucking speed, (E) overlap width and (F) depth for plucking-based power generation.

the voltage on the resistor. Figure 4A–C shows the power and energy with different configurations. The results first indicate that the compliant structure increases the power generation compared with non-compliant structures (i.e., Figure 4A, number of bridge pairs = 0). We further eliminate less effective designs such as those prone to breaking after a few uses (i.e., angles>22 degrees, length>8.22 mm). We finally adopted a two-bridge design with 0.5 mm thickness, 7.72 mm length, and 20-degree tilting angle as the optimal design for the subsequent application development.
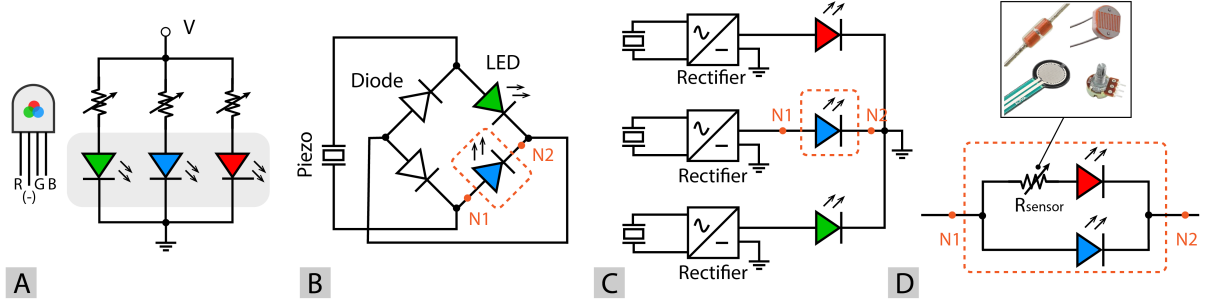
Figure 5: Circuit diagrams illustrating (A) a conventional RGB LED setup, (B) LED-as-rectifier approach, and (C) plucking-based color generation. (D) Resistive sensors in LED branches with lower turn-on voltages can enable different color combinations. Nodes $N1$ and $N2$ can be connected to the corresponding nodes in (B) or (C) to enable color changes in the respective branch.

## 3.2 Plucking-Based Power Generation

Plucking interaction can occur between two moving parts, one arranged with a plectrum and the other with a piezo element as a cantilever [40]. There are two steps in the plucking process: contact phase and release phase [23]. Our experiment revealed that LED illuminates at the transition between these two phases, while during the initial stage of contact and the final stage of release, the voltage remains below the LED's ON voltage, keeping it from illuminating to a visible state. We used a *Soft Piezo* for plucking-based power generation, for its small size (10 mm diameter), thinness (0.1 mm), and low stiffness [58], as shown in Figure 3D.

To understand the effect of different forms of plectrum and plucking behaviors on power generation, we conducted a study. Specifically, we explored three parameters, including plucking speed, overlap depth and width between the plectrum and the piezo. Considering the subtle differences between parameters, we leveraged a motorized plucking setup, as shown in Figure 3B, driven by a speed-controlled DC motor to perform consistent plucking actions on the soft piezo to eliminate variability from manual input. We used the same measurement setup as discussed in Section 3.1. For each configuration, we 3D printed its module and conducted ten plucking trials. Figure 4D–F shows the power generation with different configurations. We found that power and energy remain relatively unchanged across different speeds and widths, but increase with greater overlap depth, due to the larger deformation caused by deeper insertion. However, larger deformations tend to more easily break the piezo element, and thus we eventually adopted the 3 mm overlap depth and 2.5 mm width design for our application development for a good balance of power generation and durability in our research prototypes. From our study, the plucking-based mechanisms produce a higher current, resulting in an increased LED light intensity compared to striking-based power generation.

## 4 INFORMATION ENCODING

Our data encoding avoids oscillators or any digital components and instead relies solely on the movements of the power generator driven by user interactions to induce sequential LED illumination. However, movements during interactions vary over time and differ among users, resulting in an unknown and inconsistent LED blinking amplitude and frequency. These challenge the effectiveness of the most common modulation schemes utilized in VLC, including On-Off Keying (OOK) and Frequency Shift Keying (FSK), which depend on oscillators to generate specific clock signals to modulate the transmitted signals, and precise timing between the camera and LED to decode information (e.g., distinguishing the number of consecutive "0"s from the duration of LED "off" states). In response, we adopt Color Shift Keying (CSK) modulation for information encoding, embedding data the colors of actively emitted LEDs. Colors are more tolerant of power fluctuations caused by varying user inputs, and less sensitive to environmental variations such as ambient brightness, making them easier to denoise and decode. By utilizing a combination of colors, CSK enables higher data rates through the transmission of multiple data bits per symbol [46]. Specifically, *LuxAct* employs a 3-CSK constellation with a ternary data representation – Red (R) = 0, Green (G) = 1, and Blue (B) = 2.

## 4.1 Activity-Sensitive Color Generation

*4.1.1 Principles of operation.* The principle behind RGB LEDs generating different colors lies in controlling the intensity ratios of the red, green, and blue channels, and combining them to produce a full spectrum of colors. Figure 5A illustrates a conventional circuit where varying the resistance in each color branch allows for color adjustment. As the resistance in one branch increases, the intensity of the corresponding color channel decreases. Our goal is to map interactive inputs (i.e., striking or plucking piezos) and environmental signals represented by resistive changes, into color changes, without relying on microcontrollers and with minimal electronics. With this objective in mind, we adopted the following approaches:

First, for striking-based power generation, we used LEDs as components of a rectifier, where different colors are illuminated at different current directions, as illustrated in Figure 5B. This method is useful in AR contexts, where POV cameras often struggle to differentiate between hovering, resting, and actual pressing hand gestures on surfaces. Forming these interaction-powered, dot-sized visual indicators into ultra-low-cost, disposable fingertip wearables, or embedding them onto object surfaces can help cameras to detect touch inputs and discrete press-and-release events more reliably.
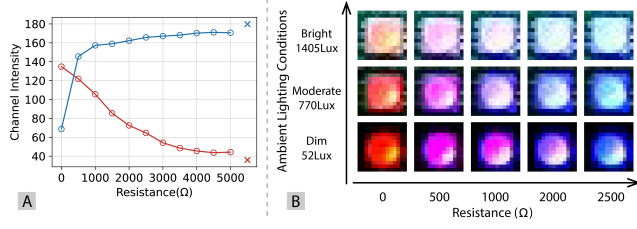
**Figure 6: Validation study of color changes with resistance. (A) Red and blue channel intensity varying with resistance in the red LED branch. The cross marker is the channel intensity measured from an illuminated blue LED. (B) RGB images of LED captured under different lighting conditions, with different resistance in the red LED branch.**

Second, for plucking-based power generation, we used the circuit shown in Figure 5C, where each piezo independently generates power for a specific color. Unlike the first approach, which allows a single piezo to produce two colors, this method produces one color per piezo, making it less material-efficient. However, it provides greater flexibility in generating longer and more dynamic color sequences (i.e., higher information capacity), as the color sequences are derived from the order in which the piezos are plucked, instead of the direction of current flow. It also enables a broader design space for translating diverse interactive motions into color changes, such as twisting and sliding, beyond touching and pressing motions.

To broaden the space of activity-to-color mappings for representing a more diverse set of sensory data, we drew inspiration from the fundamentals that varying the resistance in each R, G, B branch can alter the resulting color. We leverage resistive sensors in series with different color channels to create combinations of colors to convey sensing information. We use the red and blue channels as an example to illustrate this approach in Figure 5D. Specifically, when $R_{sensor} = 0$, only the red LED turns on, due to the inherent difference in ON voltage between red and blue LEDs (typically $v_r < v_b$). When $R_{sensor}$ increases, the red intensity decreases and the blue intensity increases. When $R_{sensor}$ approaches infinity (i.e., open circuit), only the blue LED turns on. We incorporate a more detailed analysis in Appendix A.2. Visually, the color of the RGB LED shift from red to blue as $R_{sensor}$ increases, and this color information can be utilized to infer sensor data such as applied force or temperature.

*4.1.2 Validation Study.* To validate the color changes with varying resistance and identify the effective resistance range, we conducted a study with the same motorized plucking mechanisms we introduced in Section 3.2. We varied the resistor in the red LED branch from 0 to 5kΩ in a stationary setting, under three light conditions, and recorded the LED images. We then compute the average intensity of the raw R and B channels within the LED region, Figure 6A shows the result, with partial image examples shown in Figure 6B. We observed that for the soft piezo, the most sensitive range occurs below 2kΩ, where red intensity decreases while blue intensity increases rapidly. At a higher resistance range, the color changes are less drastic. In our subsequent application development that uses plucking-based power generation, we empirically chose resistive sensors that operate within 0-2kΩ to meet the sensing objective. We followed a similar procedure to determine the resistance

range that yields the most distinct color changes for the rigid piezo in striking-based applications, which was identified as 0–250 kΩ from our experiments. This calibration accounts for the different power generation capabilities between the two piezos. Please refer to Appendix A.2 for more information.

## 4.2 Information Packaging

*4.2.1 Static Information.* In our context, static information refers to data that does not change with the underlying interactions, such as the identification (ID) information found in barcodes and markers. *LuxAct* offers a similar capability, in which object-embedded IDs are triggered and transmitted only upon interactions, rather than being constantly broadcast to cameras. Thus, the existence of *LuxAct* signal serves as a strong indicator of the presence of user interactions. We generate our own ID database for feasibility study. Specifically, for an ID of length $L$, we generate all $3^L$ sequences and assess them through circular uniqueness checking in both the forward and reverse directions and eliminate conflicted IDs. This is because interactions with an object can start from any position in either direction. In our applications (Section 6.2), we used a 4-digit ID, resulting in a total of 21 unique combinations in the database. The number of IDs grows nearly exponentially with $L$; for instance, an 8-digit ID yields a database of 498 unique entries, demonstrating the potential of *LuxAct* for scalable object identification. Figure 7C shows an example of color channel intensities measured from the opening and closing of a hinge box embedded with an ID of RGBG.

*4.2.2 Sensing Information.* Section 4.1 discussed the generation of activity-sensitive colors. However, to enable tracking and information decoding, the color symbol must also be appropriately packaged for transmission. Besides the R, G, B color symbols, we denote an additional symbol "X" for embedding sensing information. Due to variations in ambient lighting, relying on a single symbol to decode sensing information can lead to inaccuracies. To address this, we arrange a reference symbol alongside "X" to assist in interpreting the sensing bit. For example, when embedding sensing information using the red and blue channels, we structure the symbols as "RX", where "R" serves as the reference color. This approach derives from the insight that the ambient lighting conditions affect both the R and X symbol similarly, as seen in Figure 6B. The difference in color channels between "R" and "X" is leveraged to retrieve the sensing information, which we will detail in Section 5.5. Note that these sensing symbols can be embedded in data sequences such as an ID, uniting our two information packaging approaches to enhance everyday objects with both identification and sensing capabilities. Figure 7D shows an example of color channel intensities measured from rotating a knob (GXR) from 0° to 360°, resulting in a total of six transmitted packets. The color intensities of "X" sensing bit vary with positions accordingly.

## 4.3 Encoder Module Design

Once we design a color sequence, the next task is to integrate it into a piezoelectric power generator. For striking-based power generation, the color sequence is encoded by the rectifier. For plucking-based power generation, the encoder consists of two modules: the plectra module and the piezo cantilever beam holder, the relative
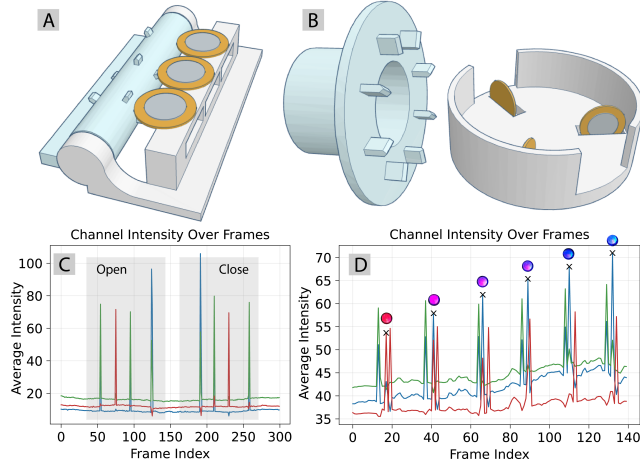
**Figure 7: Modules and signals. (A) Encoder module of the hinge box embedded with RGBG packet using $M$-$M$ configuration, and (C) signals measured from opening it to 90 degrees and closing. (B) Encoder module for the knob embedded with a GXR packet using $1$-$N$ configuration, and (D) signals measured from a 0º to 360º rotation. The cross markers are signals from the sensing bit "X".**

motion of which generates power and illuminates the LED sequentially. Based on whether each piezo beam interacts with a shared plectra module or with separate plectra modules, we employed two configurations: $1 - N$ and $M - M$, where $N$ is the length of the color sequence and $M$ is the number of symbols determined by modulation constellation (M=3 in *LuxAct*). Similar plucking-based encoder module design can be found in prior work that converts motions on structured modules into identifiable acoustic signals [28, 62] and RF backscatter [34, 35].

*4.3.1 $1 - N$.* With this configuration, a single plectra module interacts with $N$ piezo beams, and the information is embedded in the spatial arrangement of the piezo beams. The piezo beams are evenly spaced at intervals of $2\pi/N$ radians, while a total number of $K$ plectra are arranged every $2\pi/K$ radians. In our research, we ensure that $gcd(N, K) = 1$ so that only one piezo beam is plucked every $2\pi/NK$ radians. The information can be fully retrieved after $2\pi/K$ radians of interaction. Figure 7B illustrates the design with a knob as an example (N=3, M=3, K=8). Of note that for the same color sequence, the spatial arrangement of piezo beams is determined by both $N$ and the design parameter $K$, as successive plucking positions are not necessarily spatially adjacent.

*4.3.2 $M - M$.* With this configuration, $M$ plectra modules interact with $M$ piezo beams independently. The $N$-length color sequence is split across the $M$ number of plectra modules. Figure 7A illustrates the design of a hinge as an example. The arrangement of the plectra determines the order of the piezo being activated. Compared with the $1-N$ configuration, in which a greater amount of piezo elements are required as the length of the color sequence increases, this approach only uses $M$ piezos to transmit $N$ length of information, making it more efficient in terms of piezoelectric material usage.
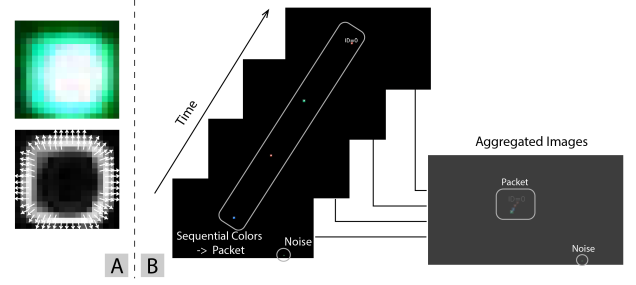


**Figure 8: LED visualization. (A) Example of a green LED (top) and its $\theta_L$ map and gradient vectors $G_{\theta_L}$ (bottom). (B) Temporal and spatial representation of LED tracking across frames. Only candidate regions with temporal and spatial correlation are detected as LED sequences (i.e., a packet), while others are discarded are noise.**

## 5 INFORMATION DECODING

In an AR setting, both POV cameras and objects manipulated by hands move continuously and unpredictably, which can introduce numerous LED candidates with simple frame differencing approaches. The shape of LEDs can be distorted during an interaction due to the changes in viewing angle and motion blur, which makes techniques that rely on the assumption of a fixed LED shape less effective. In light of these challenges, we present an approach that couples the temporal and spatial variation in both brightness and color to detect LEDs with CSK demodulation. Our algorithm is developed in the CIELab color space, which has shown enhanced capability in decoding CSK symbols by separating brightness and color information into the luminance channel ($L$) and two chromatic channels ($a$: green-to-red, $b$: blue-to-yellow) [30].

### 5.1 Temporal Filter

We first calculate the color differences between the two frames by $\Delta E = \sqrt{\Delta L^2 + \Delta a^2 + \Delta b^2}$, where $\Delta\cdot$ represents the difference in the corresponding channel. A high-pass filter is then applied to $\frac{\Delta L}{|\Delta L|}\Delta E$ to identify the regions that have an increasing brightness and significant color changes. This is based on the observation that the transition of an LED from an OFF state to an ON state is highly distinctive in the environment due to simultaneous changes in both color and brightness. This approach can distinguish the LED from some blurry edges caused by the camera or object motion. We then apply a dilation followed by an erosion to close the small gaps due to uneven $\Delta E$, and expand the resulting areas to bounding rectangles for further analysis.

### 5.2 Spatial Filter

Compared with moving objects, light sources exhibit a distinctive characteristic: they appear brightest at the center and gradually fade toward the edges due to the decrease in brightness as the angle between the receiver and the light source increases. Spatially, this appears as the decrease in the Luminance-Chroma angle $\theta_L$ toward the center, where $\theta_L = \cos^{-1}(L/\sqrt{L^2 + a^2 + b^2})$. We compute the gradient of $\theta_L$, $G_{\theta_L}$, to find the radial distribution in each bounding
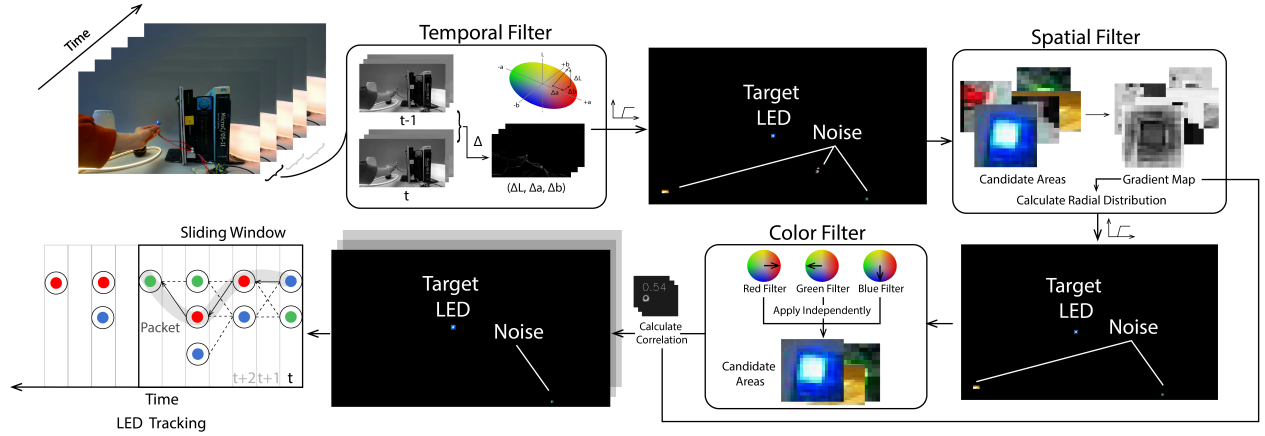
**Figure 9: An overview of our signal processing pipeline, including temporal filter, spatial filter, color filter, and LED tracking.**

rectangle. Figure 8A shows an example. Following the approach in [16], we define the Luminance-Chroma Outwardness (LCO) to quantify this distribution,

$$LCO = \frac{1}{NP} \sum \frac{\vec{g}_{x,y} \cdot \vec{d}_{x,y}}{|\vec{d}_{x,y}|} \quad (1)$$

where $\vec{g}_{x,y}$ and $\vec{d}_{x,y}$ are the gradient vector and the directional vector at pixel $(x, y)$, and $NP$ is the number of pixels in the candidate area. We then applied a high-pass filter to eliminate candidate areas that have negative $LCO$ since these areas do not exhibit the illuminative properties of light sources.

### 5.3 Color Filter

Color filters are constructed according to the CSK constellation. In a-b plane, we initialize the three color filters as $\vec{F}_r = (1, 0)$, $\vec{F}_g = (-1, 0)$ and $\vec{F}_b = (0, -1)$, and apply them independently to each candidate area by doing $FC = \vec{F} \cdot \vec{c}$, where $\vec{c}_{x,y} = (a_{x,y}, b_{x,y})$ is the chroma values at each pixel $(x, y)$. For an illuminated light source, the decrease of brightness results in an increase and then a decrease in chroma $\sqrt{a^2 + b^2}$, forming a halo if the colored LED exists. Visually, the color of the LED is more prominent at the boundary, whereas the center tends to be overexposed (white-ish). We then calculate the correlation between the gradient map and each $FC$, and the color is determined by finding max $\left\{ \text{corr}(G_{\theta_L}, FC_i) \mid i \in \{r, g, b\} \right\}$. The rationale behind is that when the color halos align with the brightness changes, the likeness of an illuminated LED with the filtered color is the highest.

### 5.4 Tracking Target LED

After the above processing, we identify a series of candidates $S_f = \{s_1, s_2, ...\}$ at different positions at each frame, where $f$ is the frame index and $s_i = ((x_i, y_i), c_i)$ represents position and color information. We observed that, except for the target LED, other candidates (noise) do not have strong spatial or temporal correlations with themselves, including randomly blinking light sources. Figure 8B illustrates the idea. To track the LED, we apply a sliding window to the continuous frames to narrow down the search space for more efficient computing. We construct a graph for all candidates within

the window, with edges generated between $s_i \in S_{f_m}, s_j \in S_{f_n}, m \neq n$ when meeting the spatial and temporal proximity criteria. We then adopt Depth First Search (DFS) to find clusters. Finally, the color sequence formed by candidates within each cluster is examined— clusters that exhibit specific color orders are recognized as LED packets while the rest are discarded as noise. The LED tracking in Figure 9 illustrates this flow. This tracking approach inherently allows the detection of multiple color sequences simultaneously. The tracking process is followed by decoding to interpret the packet data.

### 5.5 Decoding

To decode the *static information* (i.e., ID), we use the detected color sequence and search across the database to find the matching sequence. To decode the *sensing information* (i.e., the corresponding sensor value mapped to symbol "X"), we employ a differential color intensity analysis. We use the red and blue channels as an example to illustrate this approach, where the reference symbol is R and X is formed by the combination of R and B colors. Specifically, we define the differential color ratio as:

$$Y = \alpha \frac{R_X}{R_R} + (1 - \alpha) \frac{B_R}{B_X} \quad (2)$$

where $R_X$ and $B_X$ are the red and blue channel intensities of the sensing symbol and $R_R$ and $B_R$ are those for the reference symbol, and $\alpha \in [0, 1]$ is the weight factor to compensate the camera sensitivity to different colors. We experimentally set the value to 0.8. While decoding data from raw R, G, B values under varying lighting is challenging, the R symbol serve as a reference point to infer red and blue color intensity in the X symbol and thus the sensing information. Given the feature input $Y$, the target sensing status can be estimated using a pre-trained polynomial regression model or a calibration table, depending on the overall system design. While being evaluated in our studies, this feature selection is preliminary and can be further refined in future work.

### 5.6 Validation Study

*5.6.1 Performance Under Ambient Light Changes.* We conducted an experiment to validate the capability of our camera in differentiating
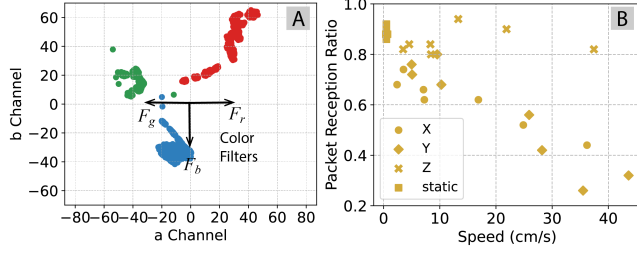
Figure 10: Validation studies. (A) R, G, B LEDs captured by cameras under different lighting conditions. Color filters are denoted as $\vec{F}_r$, $\vec{F}_g$, $\vec{F}_b$ for the three colors. (B) Packet reception ratio varying with LED motion speed.
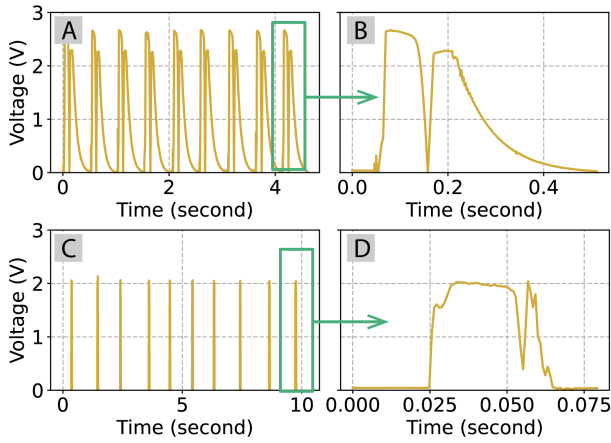


Figure 11: Frame rate validation. (A) shows the voltage of LED with striking-based power generation, with (B) showing a zoomed-in view. (C) shows the voltage measured from plucking-based power generation, with (D) showing a zoomed-in view.

color symbols (i.e., red, green, blue) under different ambient lighting conditions. We used a desk lamp to shed light of different brightness on a powered RGB LED, and used a static camera to record a 10-second video in each condition. Figure 11A shows the result in a-b plane of the CIELab color space. As ambient lighting becomes very bright or very dark, the LED appears more desaturated or white to the camera, represented as a, b values approaching to zeros. Red color exhibits the most noticeable changes compared to blue and green, likely due to the different sensitivities of our camera to different colors. Nevertheless, the three colors have a clear clustering under different lightings, which can be identified by color vector multiplication (Section 5.3). Instead of relying on absolute color values for LED tracking, our approach requires cameras to distinguish the three colors when they appear, a ability inherently possessed by RGB cameras. While ambient lighting affects the absolute values of colors, it has little effect on the clustering.

*5.6.2 Performance Under Motions.* In this study, we investigate the performance of our detection pipeline in tracking data packets under motions. We mounted a powered RGB LED on an iPhone,

configured to transmit a repeating RGBG packet sequence, with each LED pulse blinking at 10 Hz (25 ms ON time). The iPhone concurrently recorded its 3D trajectory using ARKit, from which we can compute the velocity. An experimenter held the phone 45 cm from the camera, stationary or moving it along one of the three axes (X, Y, or Z) in each trial, using a different speed each time. For each trial, 50 packets were transmitted, and the number of packets successfully received by the camera was recorded to calculate the packet reception ratio. Results are presented in Figure 10B, which indicates that detection performance declines when the LED is in motion (e.g., exceeds 25 cm/s). Among the motion conditions, movement along the Z-axis (i.e., vertical to the camera) resulted in the highest packet reception ratio, likely because Z-axis motion most closely resembles stationary behavior from the camera's perspective.

*5.6.3 Frame Rate Validation.* To validate the ability of our cameras operating at 30 FPS to capture interaction-powered LED impulses, we conducted validation experiments. We used the same striking and plucking setup as used in previous studies (Figure 3), and measured the voltage of LED using an oscilloscope configured at 0.8 ms time resolution (1.25 kHz sampling rate). Figure 11A-D illustrates the results. Striking the piezo results in a longer LED ON duration (~45 ms) compared to the plucking mechanism (~20 ms). Additionally, we used a micro-controller to control an LED blinking at 10 Hz with an ON duration of 1 ms, 10 ms, 20 ms, and 30 ms, and found that our 30 FPS camera can capture an average of 40.0%, 92.5%, 97.5%, and 100% of the blinks. These experiments validated that our current setup is sufficient for detecting LED blinks.

## 6 APPLICATIONS

In this section, we demonstrate the design of various use cases enabled by *LuxAct*. We report the implementation details, evaluation study and results of each application. For a detailed overview of the circuit connections used in each application, refer to Appendix A.1.

### 6.1 Overview

*6.1.1 Hardware and Configuration.* Figure 12 shows our hardware. We created a simple circuit board that contains three rectifiers (KMB24F) for the three color channels, simple interfaces to connect resistive sensors, and a tri-color LED (QLSP29RGB, 5050). Appendix A.1 provides a detailed wiring layout of the circuit board. All mechanisms were 3D-printed and retrofitted into objects. On the



Figure 12: Hardware. (A) Front side and (B) back side of our circuit board. (C) Camera mounted on an AR headset.
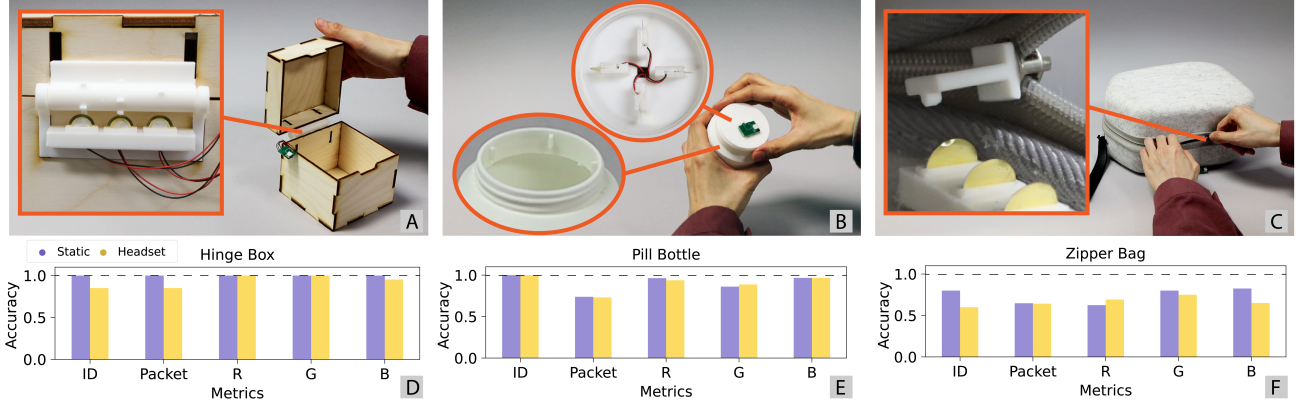
**Figure 13: Object identification. Prototypes of (A) hinge box, (B) pill bottle, and (C) zipper bag. (D)-(F) Evaluation results for the corresponding objects at the first row.**

receiver side, we used the ELP-USB48MP02 camera module for its wide angle and high color fidelity. The camera was mounted on a headset tilting down 45°. The images were streamed to a laptop and processed with OpenCV. The frame rate was set to 30 FPS [1].

*6.1.2 Evaluation Procedure.* The evaluation was carried out in a lab environment, except for the faucet adapter, tested in a bathroom, and the barrel cranker, tested in an indoor setting equipped with a water supply and draining system. One complete set of data collection sessions involves an experimenter performing ten interaction trials while wearing the camera-mounted headset. Each trial involves activities such as opening and closing an object, pressing on a surface, and releasing and cranking for one cycle, during which one or more packets can be transmitted depending on the object design. Meanwhile, other than the camera mounted on the headset, a second camera was positioned stationary around 50 cm away from the objects to capture data as a baseline for comparison with mobile settings. For each application, we conducted two complete data collection sessions at different times (i.e., training and testing). All evaluation results were obtained from regression models calibrated using data from the training session and tested on data from the testing session.

*6.1.3 Evaluation Metrics.* Each object was embedded with a known color sequence, which was transmitted a set number of times during one interaction trial. With our decoding algorithm, the detected color sequences were searched and matched across all possible IDs that are mutually unique as discussed in Section 4.2. For identification applications, we leveraged ID, packet, and symbol accuracy to evaluate the detection performance. For each trial, the ID is determined by majority voting among the set of detected packets. The packet accuracy is calculated by the ratio between the total number of correct IDs and the total number of detected packets. For further analysis, we manually examined the images to count the number of correctly detected symbols for each color symbol. For sensing applications, we first detected the color sequence throughout each trial of data using our tracking algorithm, and then extracted the

sensing bit from the sequence. We then use all sensing bits at different statuses from the training session to fit a polynomial regression model, and then evaluate it with data from the testing session by calculating the mean absolute error (MAE).

## 6.2 Object Identification

Similar to QR codes and barcodes, *LuxAct* encodes static information into everyday objects beyond their visible appearances. Digitalizing objects in this way enables an interactive, context-aware AR experiences. For example, an AR cooking assistant recognizing each sauce container as the user twists it, can offer real-time guidance through a recipe. We identify three representative mechanical structures commonly found in daily objects that generate motions when interacted with by users, including hinges, caps, and zippers. Figure 13A–C show our design of a hinged box, a pill bottle, and a zipper bag featuring the aforementioned mechanical structures, and this design can be generalized to a broader range of objects that share similar components. For the hinge box, we integrate plectra and piezos into the moving and stationary parts of a hinge. For the pill bottle, the plectra are on the threading area of the bottle, and the piezos are on the cap. For the zipper bag, a plectrum is attached to the inner side of the zipper tab, while the piezos are positioned on the sides. The color sequences for hinge box, pill bottle, and zipper bag are RRGB, RGBG, and RGBB in our prototypes.

We conducted two data collection sessions for each object under two lighting conditions (measured 324 Lux and 782 Lux). The results, as seen in Figure 13D–F show that the detection of the hinge box outperforms that of the other, mainly due to their little movement during interaction. For the pill bottle, during one trial of interaction (opening and closing), multiple packets are transmitted, therefore the ID detection rate for is high despite a certain number of false packets are detected. The zipper bag has the poorest performance, mostly for the current single-packet implementation lacking redundancy for reliable detection, which can be improved by increasing the number of packets in future designs. We did not observe significant differences between the headset camera and the baseline static camera, nor among the different color symbols.

---

[1] Gamma correction was disabled. Auto exposure was disabled and set to -5 . All other settings use default configurations in the ELPCAP software.
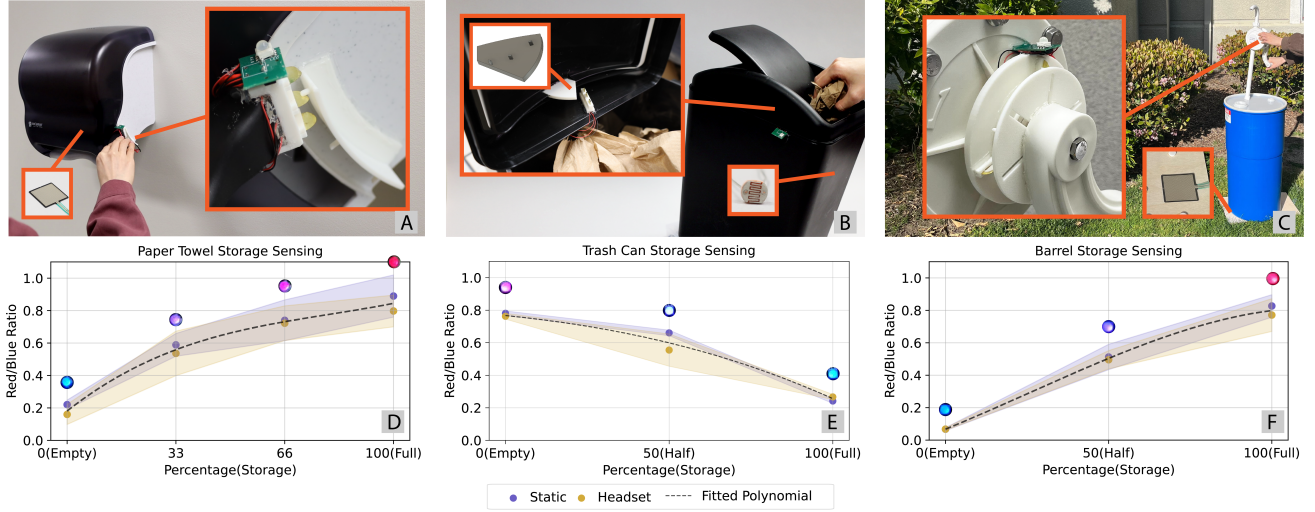
**Figure 14: Storage sensing. Prototypes of (A) paper towel dispenser, (B) trash can, and (C) barrel hand crank. (D)-(F) Evaluation results for the corresponding objects at the first row. The LED images are illustrative examples captured at each corresponding status from the camera in stationary settings. We followed the same annotation convention throughout the paper.**

## 6.3 Storage Sensing

Monitoring the status of resources enables automatic alerts and proactive management, which, however, remain challenging for cameras due to the limited, or complete absence of visible cues. Building on the insights that the presence of user activities in the environments often drives the most changes in resource storage, we showcase the potential of *LuxAct* for interaction-powered storage monitoring. We developed three applications (Figure 14A-C) by choosing appropriate type of resistive sensors and embedding them strategically within storage mechanisms. While the encoding scheme is compatible with the object identification approach described in the previous section, we chose the color sequence GRX for these applications for simplicity.

*6.3.1 Paper Towel Storage Sensing.* We installed the plucking mechanism on the dispenser handle (Figure 14A), which can generate power when pressed by users. Inside the dispenser, two Force Sensitive Resistor (FSR) are connected in parallel, and a 3D printed piece is used to focus the force onto the pressure sensors. We used three rolls of paper towels at different weights (1.63 kg, 1.12 kg, and 0.65 kg) to vary the status of paper remaining (3/3, 2/3, and 1/3), which resulted in a resistance of 1785 Ω, 896 Ω, and 347 Ω measured in the FSR. An empty status was also tested (FSR measured >20 MΩ). The lighting conditions at the two sessions of data collection were measured at 216 Lux and 515 Lux, respectively. Figure 14D shows the different colors we detected in different statuses measured as percentages (0–100%). On average, we got an average MAE of 2.09% (SD=1.24), 13.32% (SD=8.26), 9.85% (SD=7.12), and 11.94% (SD=8.17) for the four storage statuses.

*6.3.2 Trashcan Remaining Capacity Sensing.* We mounted the plectrum module on the rotational lid, the piezos along the side of the lid, and two Light Dependent Resistor (LDR) on the body of the trash can (Figure 14 B). When users press the lid, the light is directed into the trash can, where varying levels of fill can obstruct the light from the sensors at different heights. The two LDRs were connected in parallel, with one positioned at the half-filled level and the other at the full level near the lid. This setup results in resistances of nearly infinity, 1021 Ω, and 531 Ω at the three storage levels (full, half, empty). Figure 14E shows the result, with data collected under indoor lighting conditions of 667 Lux and 892 Lux. We calculated an average MAE of 5.15% (SD=3.19), 9.12% (SD=8.10), and 2.31% (SD=1.86) for the three storage statuses.

*6.3.3 Water Storage Sensing.* We retrofitted our plectrum module and piezos into a hand crank of a 15-Gallon rain-collecting barrel (Figure 14C). We placed a wooden board underneath the barrel and then used 60 small plastic cylinders (12mm×12mm×2mm) to distribute the weight of the water and adapt to the sensing range of our FSR. We used an FSR below one of the cylinders to measure the force generated by different water levels. We varied the water storage with empty, half (~60 lbs), and full (~120 lbs), at which the resistance of the FSR was measured at >20 MΩ, 1026 Ω, and 320 Ω. Figure 14F shows the plot. We calculated an average MAE of 0.28% (SD=0.16), 7.40% (SD=6.12), and 8.33% (SD=9.38) for the three storage statuses.

## 6.4 Ubiquitous Interactors

Battery-free interactors enable ubiquitous user input throughout the environment [10, 71, 77, 87]. We demonstrate the potential of designing *LuxAct* into input interfaces through two representative interactors—a push button and a knob (Figure 15A and 15B).

*6.4.1 Push Button.* We utilized the compliant structure to enhance the striking effect of the piezo surface to increase the generated power, and the LED-as-rectifier approach to generate color sequence in this application. The color sequences are B (press) and
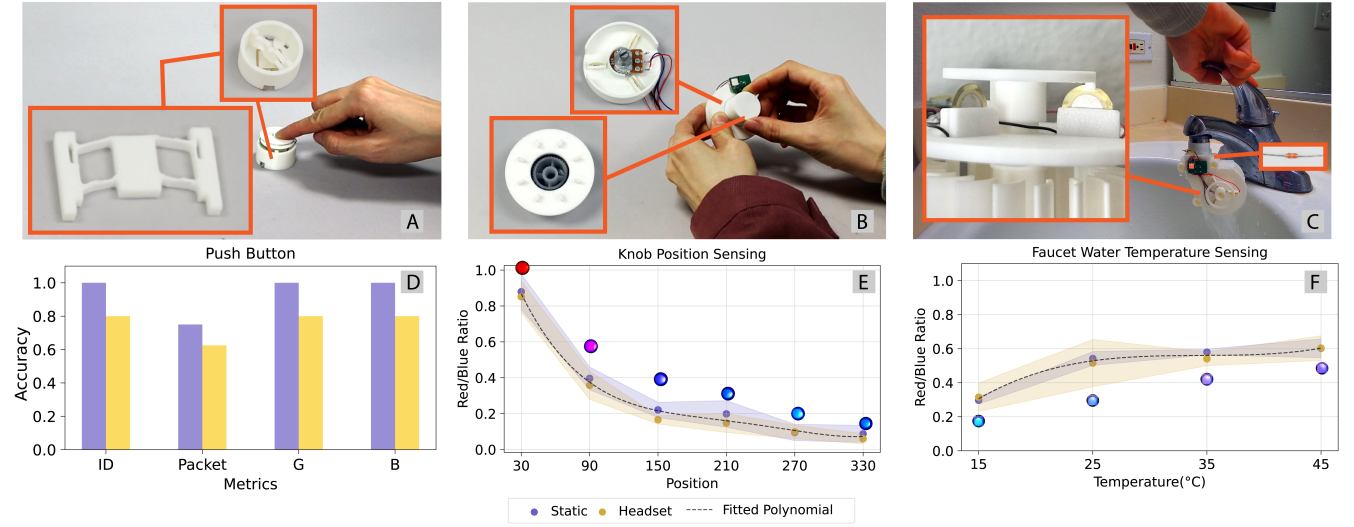
**Figure 15: Devices and evaluation results. (A) Push button. (B) Knob. (C) Faucet adapter. (D)-(F) Evaluation results for the corresponding objects at the first row.**

G (release). Figure 15D shows the results for the two evaluation sessions (189 Lux and 488 Lux), where we pressed the buttons ten times each. The result indicates that the static camera can capture all button activations, whereas the headset camera missed 4 out of 20 trials, as motions from the headset camera led to a moderate reduction in detection accuracy.

*6.4.2 Knob.* We embedded a 2 kΩ potentiometer into the knob to change the resistance in the red LED branch for absolute position sensing. We divided the 360-degree knob into six sections, each containing a packet containing an "X" sensing symbol that varies with the resistance. The color sequence in one packet is GXR. Figure 15E shows the evaluation result from two data collections (221 Lux and 687 Lux). With our testing trials, the MAE for the six positions is 2.91º (SD=2.46), 7.96º (SD=9.46), 12.24º (SD=8.95), 13.16º (SD=4.01), 15.21º (SD=10.69), and 38.71º (SD=11.29). The results indicate that the system performs well at lower positions (<150º) but degrades significantly at higher positions(>210º), as the color change at the higher positions was not as apparent as at lower positions, leading to increased estimation errors. These results suggest that a potentiometer with a narrower resistance range is highly likely to yield greater accuracy.

## 6.5 Environment Sensing

*6.5.1 Sensor "Tags".* Sensing environmental factors such as temperature and humidity has a direct impact on people's comfort and well-being. To demonstrate the potential of *LuxAct* for sensing the environment, we designed a faucet adapter (Figure 15C) that harvests energy from water flow and communicates temperature information to cameras, which can then warn users about hot water to help prevent potential harm. The plucking mechanisms are co-axial with the water wheel driven by flowing water, while the piezos are stationary. A thermistor is embedded within the waterwheel to sense the temperature of water. We varied the temperature from

15°C to 45°C, with 10°C as an interval, calibrated by a digital thermometer probe. The temperature can result in a resistance change ranging from 1 kΩ to 0.5 kΩ. At each temperature, we have the water flowing for ten seconds. As shown in Figure 15F, the regression becomes less apparent as the temperature increases. This is because of the limited sensitivity of our selected thermistor within the typical faucet water temperature range (20—50°C), resulting in minimal color variation. On average, we got an MAE of 1.15ºC (SD=0.54), 6.23ºC (SD=6.90), 7.54ºC (SD=9.32), and 7.66ºC (SD=3.41) on the four temperatures. We anticipate that future work, including the use of more sensitive thermistors, will enhance the system to meet more rigorous application requirements.

*6.5.2 Finger "Probes".* With our ultra-low-cost and battery-free design, *LuxAct* has the potential of being integrated into wearables to enrich environment sensing beyond what is visible to cameras, such as temperature and conductivity. Figure 16A shows our prototypes. We used striking-based power generation and the LED-as rectifier approach for this application. At the top, we made an ortho-planar spring to provide a subtle tactile sensation on the finger, which includes a small extruder to focus the force when pressing on the piezo. Depending on the application, we attach different sensor modules to the underside of the finger probe.

*Conductivity Sensing* We created two isolated electrodes (spaced 0.5 mm apart) using copper tape on a small piece of soft gel rubber. When the two electrodes are in contact with materials with different conductivities—foam board (approximated to 30.00 kΩ/mm), carbon paint (14.90 kΩ/mm), and conductive rubber (50 Ω/mm), the sensing branch measures different resistances resulting in different colors. Figure 16B shows the results. On average, we got an MAE of 1.18 kΩ/mm (SD=0.57), 3.55 kΩ/mm (SD=2.70), and 4.92 kΩ/mm (SD=3.10) for the three materials.

*Temperature Sensing* We used a thermistor that has a rated resistance of 200 kΩ at the common room temperature 25°C. The
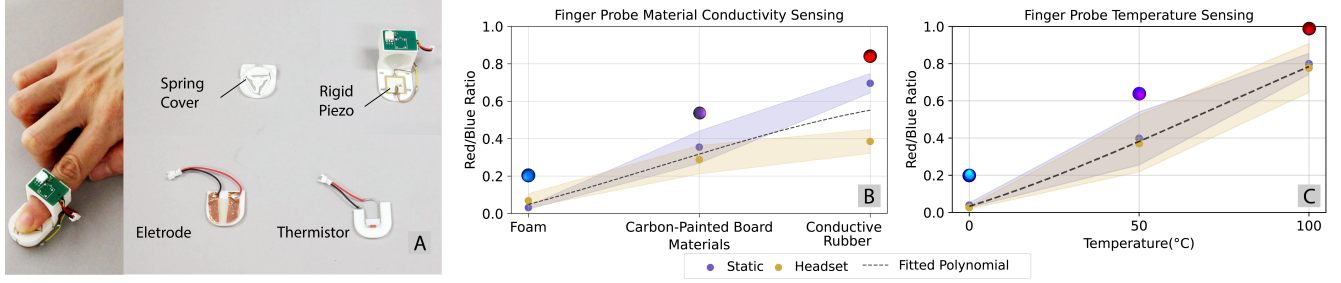
**Figure 16: Finger probe. (A) Hardware and its placement on a user's finger. (B) Evaluation for conductivity sensing, and (C) temperature sensing with the finger probe.**

resistance of the thermistor decreases as temperature increases. To evaluate the performance, we filled a metal cup with iced water (~0°C), warm water (~50°C), and boiled water (~100°C), and then wore the finger probe to touch the side of the cup. We rested our hands on the surface for 5 seconds before starting to press on it. Figure 16C shows the result. On average, we calculated an MAE of 3.19ºC (SD=1.83), 4.15ºC (SD=3.90), and 4.62ºC (SD=8.22) at the three temperatures.

## 7 DISCUSSION

### 7.1 Camera-LED Synchronization

To allow more efficient data transmission, research in VLC has developed novel sampling techniques to detect high-rate LED pulses with low-frame-rate cameras, primarily by leveraging the rolling shutter effect of cameras [15, 21]. Related studies have shown that 30 FPS cameras on commercial Android and IOS phones can decode high-speed CSK-VLC signals (blinking rates up to 1kHz) [11, 29, 30, 72, 85], This establishes a higher upper bound for camera-based LED detection and highlights the potential of POV cameras to decode longer color sequences (i.e., more information) during interaction events. In our study, we selected a 30 FPS camera for signal detection, considering the low LED blinking rates and long LED ON durations, with a reasonably reliable signal capture rate validated through experimental studies. Although beyond the scope of our current research, camera-LED synchronization is essential to ensure reliable data decoding. An investigation into how appropriate camera settings, including frame rate, shutter mode, and exposure time, can accommodate impulsive, interaction-powered LED signals remains unexplored. We anticipate future research on more efficient and effective camera-LED synchronization strategies to enhance detection performance in practical applications.

### 7.2 Camera-LED Detection in Dynamic Environments

The sensitivity of RGB cameras to visible light comes with the cost of lower robustness to dynamic settings. One challenge is the significant change of lighting conditions when users with AR smartglasses move across different environments, where colors may appear differently. Camera sensors commonly face this issue, and as a result, they are manufactured with a color correction matrix to ensure consistent color accuracy under changing lighting. Our

approach rely on detecting R, G, B colors to retrieve data, which may benefit from proper camera configurations to better handle ambient light changes, which, however, remain unexplored in our current implementation. *LuxAct* may struggle under complex, color-rich lighting where significant color distortion can occur. Future work is needed to evaluate the performance under these extreme conditions including outdoor settings with direct sunlight. On the positive side, a distinct benefit of our illuminating light markers is its capability of transmitting data under dim or dark settings, when conventional visual sensing often fails.

Another dynamic condition is motion. Even without intentional user interactions, POV cameras move with human body and continuously capture visual signals from the environment, where background objects with color may appear as if they are moving. We observed that these motions lead to an increase in candidate regions detected by our filters, adding computational overhead to the tracking algorithm. However, since these motion-induced artifacts are highly unlikely to exhibit the specific spatial and temporal patterns of encoded sequences, the false positive rate is extremely low.

During an interaction event, movements of hands and objects pose challenges for LED tracking. Background colors and objects may introduce false symbol detections, and lead to packet loss. High-speed motion can cause LEDs to blur or become spatially dispersed, making it difficult for the tracking algorithm to follow accurately. These effects are the primary contributors to the decline in performance of our system, found by validation study in Section 5.6.2. We found that the detection becomes unreliable when hand motions exceed 25 cm/s. Although moderate interactive motions such as twisting and tapping remain below this threshold, and high-speed actions like jumping or shaking are beyond our intended use case, the lack of a systematic evaluation of motion effects is a limitation of our current work. Future work should include broader testing under dynamic motion conditions, and investigate camera-LED detection strategies that can adapt to challenging motion conditions.

### 7.3 Color Generation, Encoding and Decoding

As presented in Section 4.1, we employed an empirical approach to identify the effective resistance ranges that yield distinct color changes for soft piezos and rigid piezos, and adapted our resistive sensors to operate within these ranges to enable sensing-variables-to-color mapping. Despite the visible color changes detected in our applications under different lightning conditions, as shown in the

color dots in Figure 14-16, and the monotonic relationship found by our differential decoding approach serving as proof-of-concept, a quantitative mapping among power generators, resistance and colors, and a unified calibration strategy remain unexplored. Future studies can lead to a more precise sensing-variable-to-color mapping, and thus higher sensing resolution. We envision that this mapping will be calibrated during manufacturing based on specific application requirements, as it depends jointly on the power generation capabilities of piezos, LED properties, and the resolution of the resistive sensors.

Additionally, there is still a broad design space to investigate in terms of color sequencing, encoding and decoding approach. For example, certain interaction motions such as twisting a bottle back and forth within a single packet can produce varying sequence orders, highlighting the need for sequence designs that can accommodate such ambiguities arising from interactive inputs. A denser CSK constellation diagram like 4-CSK and 8-CSK (i.e., more data embedded in one color) can increase the data rate and transmission efficiency [26]. Strategies for embedding sensing symbols into packet, and feature engineering to identify more effective representation of these symbols, are also anticipated in future work.

### 7.4 Intrusiveness and Usability

A common challenge of VLC systems is that the blinking light may cause a flickering effect, which can be intrusive to the environments and lead to visual discomfort. Prior work [29, 30] has demonstrated the elimination of flickering effect through strategic color combinations and increasing the blinking frequency—the LED will appear as a steady white light to the human eye (We observed that the RGB LED appeared steady when blinking at above 167 Hz). This may be enabled by advanced fabrication techniques that allow higher-resolution placement of plectra for high-speed plucking while maintaining a compact object size.

An alternative to mitigate perceived light flickering is utilizing infrared (IR) or ultraviolet (UV) LEDs in place of RGB LEDs. These invisible spectra have demonstrated reliable data communication capabilities as seen in TV remotes, and recently shown promise in digitalizing object interfaces [20, 22] and user interactions [39] for non-intrusive AR sensing. While our supplemental study found that the power generators in *LuxAct* are insufficient to drive IR LEDs to emit IR lights detectable by our camera (with IR filter removed), infrared light remains a promising candidate for practical applications, where different IR wavelengths (e.g., 850 nm, 940 nm) could function analogously to color channels in our system for data communication while maintaining low intrusiveness. Future work is anticipated to unlock its full potential, including investigation into interaction energy harvesting techniques compatible with IR LEDs or IR-sensitive materials, and data modulation strategies that ensure efficient communication with camera sensors.

Additionally, plucking the piezo introduces friction and sound during an interaction. With our prototypes, we did not notice significant degradation to the usability of the retrofitted object. However, our exploration of design parameters for the plucking and striking modules is still preliminary. Future work could explore designs that improve the power generation efficiency while ensuring usability.

### 7.5 Form factor

Extensive research has been done on fabricating piezoelectric materials into more flexible forms and higher power efficiency [48]. The piezos used in our prototypes are the smallest commercially available units we found that can generate enough power to illuminate LEDs with interactive input. However, these piezo elements, designed for converting resonating motions like vibrations or sounds into electrical signals for sensing, are not optimized for power generation. Future improvement may enable more efficient energy harvesting using smaller, thinner piezoelectric materials.

The fabrication resolution of the encoder module is another key factor determining the overall size of *LuxAct* devices. Higher-resolution manufacturing enables finer plectrum structures, allowing the encoder module to be more compact, which improves space efficiency and makes it possible to embed longer data sequences within smaller form factors. Materials with greater elasticity, such as metal, can be utilized to fabricate the striking mechanism to generate a higher magnitude of power while maintaining low-cost and lightweight properties. Electrically, we envision all components to be integrated into a single LED package in production, like the tiny chip within addressable LEDs.

## 8 CONCLUSION

*LuxAct* introduces a novel technique for embedding static information such as object IDs and dynamic information such as storage levels into everyday objects in a ultra-low-cost and battery-free manner. By harvesting energy using piezoelectric generators and modulating data into sequential RGB LED blinks, the system transmits information to POV cameras on AR wearables during interactions. We developed proof-of-concept power generators based on striking and plucking mechanisms using off-the-shelf piezo discs, along with first-principle encoding and decoding methods. We demonstrated 10 applications across a diverse range of passive everyday objects to communicate with cameras. With future advances in fabrication and signal processing, we envision our approach being integrated into everyday objects to enhance visual sensing capabilities and enrich AR interaction experiences.

### ACKNOWLEDGMENTS

### REFERENCES

[1] Karan Ahuja, Sujeath Pareddy, Robert Xiao, Mayank Goel, and Chris Harrison. 2019. LightAnchors: Appropriating Point Lights for Spatially-Anchored Augmented Reality Interfaces. In *Proceedings of the 32nd Annual ACM Symposium on User Interface Software and Technology* (New Orleans, LA, USA) *(UIST '19)*. Association for Computing Machinery, New York, NY, USA, 189–196. https://doi.org/10.1145/3332165.3347884

[2] Marwa Alalawi, Noah Pacik-Nelson, Junyi Zhu, Ben Greenspan, Andrew Doan, Brandon M Wong, Benjamin Owen-Block, Shanti Kaylene Mickens, Wilhelm Jacobus Schoeman, Michael Wessely, Andreea Danielescu, and Stefanie Mueller. 2023. MechSense: A Design and Fabrication Pipeline for Integrating Rotary Encoders into 3D Printed Mechanisms. In *Proceedings of the 2023 CHI Conference on Human Factors in Computing Systems* (Hamburg, Germany) *(CHI '23)*. Association for Computing Machinery, New York, NY, USA, Article 626, 14 pages. https://doi.org/10.1145/3544548.3581361

[3] Takashi Amesaka, Hiroki Watanabe, Masanori Sugimoto, and Buntarou Shizuki. 2022. Gesture Recognition Method Using Acoustic Sensing on Usual Garment. *Proc. ACM Interact. Mob. Wearable Ubiquitous Technol.* 6, 2, Article 41 (July 2022), 27 pages. https://doi.org/10.1145/3534579

[4] Abul Al Arabi, Xue Wang, Yang Zhang, and Jeeeun Kim. 2023. E3D: Harvesting Energy from Everyday Kinetic Interactions Using 3D Printed Attachment Mechanisms. *Proc. ACM Interact. Mob. Wearable Ubiquitous Technol.* 7, 3, Article 84 (Sept. 2023), 31 pages. https://doi.org/10.1145/3610897

[5] Nivedita Arora, Ali Mirzazadeh, Injoo Moon, Charles Ramey, Yuhui Zhao, Daniela C. Rodriguez, Gregory D. Abowd, and Thad Starner. 2021. MARS: Nano-Power Battery-free Wireless Interfaces for Touch, Swipe and Speech Input. In *The 34th Annual ACM Symposium on User Interface Software and Technology* (Virtual Event, USA) *(UIST '21).* Association for Computing Machinery, New York, NY, USA, 1305–1325. https://doi.org/10.1145/3472749.3474823

[6] Nivedita Arora, Steven L. Zhang, Fereshteh Shahmiri, Diego Osorio, Yi-Cheng Wang, Mohit Gupta, Zhengjun Wang, Thad Starner, Zhong Lin Wang, and Gregory D. Abowd. 2018. SATURN: A Thin and Flexible Self-powered Microphone Leveraging Triboelectric Nanogenerator. *Proc. ACM Interact. Mob. Wearable Ubiquitous Technol.* 2, 2, Article 60 (jul 2018), 28 pages. https://doi.org/10.1145/3214263

[7] Rens Bloom, Marco Zúñiga Zamalloa, and Chaitra Pai. 2019. LuxLink: creating a wireless link from ambient light. In *Proceedings of the 17th Conference on Embedded Networked Sensor Systems* (New York, New York) *(SenSys '19).* Association for Computing Machinery, New York, NY, USA, 166–178. https://doi.org/10.1145/3356250.3360021

[8] Rens Bloom, Marco Zuniga, Qing Wang, and Domenico Giustiniano. 2019. Tweeting with Sunlight: Encoding Data on Mobile Objects. In *IEEE INFOCOM 2019 - IEEE Conference on Computer Communications.* 1324–1332. https://doi.org/10.1109/INFOCOM.2019.8737410

[9] Tara Boroushaki, Maisy Lam, Laura Dodds, Aline Eid, and Fadel Adib. 2023. Augmenting Augmented Reality with {Non-Line-of-Sight} Perception. In *20th USENIX Symposium on Networked Systems Design and Implementation (NSDI 23).* 1341–1358.

[10] Daniel Campos Zamora, Mustafa Doga Dogan, Alexa F Siu, Eunyee Koh, and Chang Xiao. 2024. MoiréWidgets: High-Precision, Passive Tangible Interfaces via Moiré Effect. In *Proceedings of the 2024 CHI Conference on Human Factors in Computing Systems.* 1–10.

[11] Hao-Wei Chen, Shang-Sheng Wen, Xing-Lin Wang, Ming-Zhu Liang, Mu-Yun Li, Qing-Chang Li, and Yun Liu. 2019. Color-shift keying for optical camera communication using a rolling shutter mode. *IEEE Photonics Journal* 11, 2 (2019), 1–8.

[12] Wenqiang Chen, Yexin Hu, Wei Song, Yingcheng Liu, Antonio Torralba, and Wojciech Matusik. 2024. CAvatar: Real-time Human Activity Mesh Reconstruction via Tactile Carpets. *Proc. ACM Interact. Mob. Wearable Ubiquitous Technol.* 7, 4, Article 151 (Jan. 2024), 24 pages. https://doi.org/10.1145/3631424

[13] Jedol Dayou and Man Sang Chow. 2011. Performance study of piezoelectric energy harvesting to flash a LED. *International Journal of Renewable Energy Research* 1, 4 (2011), 323–332.

[14] Jasper de Winkel, Vito Kortbeek, Josiah Hester, and Przemysław Pawełczak. 2020. Battery-Free Game Boy. *Proc. ACM Interact. Mob. Wearable Ubiquitous Technol.* 4, 3, Article 111 (sep 2020), 34 pages. https://doi.org/10.1145/3411839

[15] Trong-Hop Do and Myungsik Yoo. 2016. Performance analysis of visible light communication using CMOS sensors. *Sensors* 16, 3 (2016), 309.

[16] Trong-Hop Do and Myungsik Yoo. 2019. A multi-feature LED bit detection algorithm in vehicular optical camera communication. *IEEE access* 7 (2019), 95797–95811.

[17] Mustafa Doga Dogan, Faraz Faruqi, Andrew Day Churchill, Kenneth Friedman, Leon Cheng, Sriram Subramanian, and Stefanie Mueller. 2020. G-ID: Identifying 3D Prints Using Slicing Parameters. In *Proceedings of the 2020 CHI Conference on Human Factors in Computing Systems* (Honolulu, HI, USA) *(CHI '20).* Association for Computing Machinery, New York, NY, USA, 1–13. https://doi.org/10.1145/3313831.3376202

[18] Mustafa Doga Dogan, Raul Garcia-Martin, Patrick William Haertel, Jamison John O'Keefe, Ahmad Taka, Akarsh Aurora, Raul Sanchez-Reillo, and Stefanie Mueller. 2023. BrightMarker: 3D Printed Fluorescent Markers for Object Tracking. In *Proceedings of the 36th Annual ACM Symposium on User Interface Software and Technology.* 1–13.

[19] Mustafa Doga Dogan, Eric J Gonzalez, Karan Ahuja, Ruofei Du, Andrea Colaço, Johnny Lee, Mar Gonzalez-Franco, and David Kim. 2024. Augmented Object Intelligence with XR-Objects. In *Proceedings of the 37th Annual ACM Symposium on User Interface Software and Technology.* 1–15.

[20] Mustafa Doga Dogan, Ahmad Taka, Michael Lu, Yunyi Zhu, Akshat Kumar, Aakar Gupta, and Stefanie Mueller. 2022. InfraredTags: Embedding Invisible AR Markers and Barcodes Using Low-Cost, Infrared-Based 3D Printing and Imaging Tools. In *Proceedings of the 2022 CHI Conference on Human Factors in Computing Systems* (New Orleans, LA, USA) *(CHI '22).* Association for Computing Machinery, New York, NY, USA, Article 269, 12 pages. https://doi.org/10.1145/3491102.3501951

[21] Alexis Duquel, Razvan Stanica, Herve Rivano, and Adrien Desportes. 2018. Decoding methods in LED-to-smartphone bidirectional communication for the IoT.

In *2018 Global LIFI Congress (GLC).* IEEE, 1–6.

[22] Martin Feick, Xuxin Tang, Raul Garcia-Martin, Alexandru Luchianov, Roderick Wei Xiao Huang, Chang Xiao, Alexa Siu, and Mustafa Doga Dogan. 2025. Imprinto: Enhancing Infrared Inkjet Watermarking for Human and Machine Perception. In *Proceedings of the 2025 CHI Conference on Human Factors in Computing Systems (CHI '25).* Association for Computing Machinery, New York, NY, USA, Article 447, 18 pages. https://doi.org/10.1145/3706598.3713286

[23] Xinlei Fu and Wei-Hsin Liao. 2019. Modeling and analysis of piezoelectric energy harvesting with dynamic plucking mechanism. *Journal of Vibration and Acoustics* 141, 3 (2019), 031002.

[24] Kristen Grinyer and Robert J Teather. 2025. ClickSense: A Low-Cost Tangible Active User Input Method Using Passive Acoustic Sensing for Mobile Virtual Reality. In *Proceedings of the Extended Abstracts of the CHI Conference on Human Factors in Computing Systems (CHI EA '25).* Association for Computing Machinery, New York, NY, USA, Article 136, 7 pages. https://doi.org/10.1145/3706598.3720000

[25] Gregory D Hager and Kentaro Toyama. 1998. X vision: A portable substrate for real-time vision applications. *Computer Vision and Image Understanding* 69, 1 (1998), 23–37.

[26] Safa Halawi, Elias Yaacoub, Saadallah Kassir, and Zaher Dawy. 2019. Performance analysis of circular color shift keying in VLC systems with camera-based receivers. *IEEE Transactions on Communications* 67, 6 (2019), 4252–4266.

[27] Chris Harrison, John Horstman, Gary Hsieh, and Scott Hudson. 2012. Unlocking the expressivity of point lights. In *Proceedings of the SIGCHI Conference on Human Factors in Computing Systems* (Austin, Texas, USA) *(CHI '12).* Association for Computing Machinery, New York, NY, USA, 1683–1692. https://doi.org/10.1145/2207676.2208296

[28] Chris Harrison, Robert Xiao, and Scott Hudson. 2012. Acoustic barcodes: passive, durable and inexpensive notched identification tags. In *Proceedings of the 25th annual ACM symposium on User interface software and technology.* 563–568.

[29] Yuki Hokazono, Koichi Hasegawa, Yoshiaki Narusue, and Hiroyuki Morikawa. 2019. Long-range flicker-free LED-to-camera communication using differential color shift keying. In *ICC 2019-2019 IEEE International Conference on Communications (ICC).* IEEE, 1–7.

[30] Pengfei Hu, Parth H Pathak, Xiaotao Feng, Hao Fu, and Prasant Mohapatra. 2015. Colorbars: Increasing data rate of led-to-camera communication using color shift keying. In *proceedings of the 11th ACM conference on Emerging Networking experiments and technologies.* 1–13.

[31] Zhizhang Hu, Amirmohammad Radmehr, Yue Zhang, Shijia Pan, and Phuc Nguyen. 2024. IOTeeth: Intra-Oral Teeth Sensing System for Dental Occlusal Diseases Recognition. *Proc. ACM Interact. Mob. Wearable Ubiquitous Technol.* 8, 1, Article 7 (March 2024), 29 pages. https://doi.org/10.1145/3643516

[32] Keiichi Ihara, Mehrad Faridan, Ayumi Ichikawa, Ikkaku Kawaguchi, and Ryo Suzuki. 2023. Holobots: Augmenting holographic telepresence with mobile robots for tangible remote collaboration in mixed reality. In *Proceedings of the 36th Annual ACM Symposium on User Interface Software and Technology.* 1–12.

[33] Muhammad Iqbal and Farid Ullah Khan. 2018. Hybrid vibration and wind energy harvesting using combined piezoelectric and electromagnetic conversion for bridge health monitoring applications. *Energy conversion and management* 172 (2018), 611–618.

[34] Vikram Iyer, Justin Chan, Ian Culhane, Jennifer Mankoff, and Shyamnath Gollakota. 2018. Wireless Analytics for 3D Printed Objects. In *Proceedings of the 31st Annual ACM Symposium on User Interface Software and Technology* (Berlin, Germany) *(UIST '18).* Association for Computing Machinery, New York, NY, USA, 141–152. https://doi.org/10.1145/3242587.3242639

[35] Vikram Iyer, Justin Chan, and Shyamnath Gollakota. 2017. 3D printing wireless connected objects. *ACM Trans. Graph.* 36, 6, Article 242 (Nov. 2017), 13 pages. https://doi.org/10.1145/3130800.3130822

[36] Junsu Jang and Fadel Adib. 2019. Underwater backscatter networking. In *Proceedings of the ACM special interest group on data communication.* 187–199.

[37] Hiroki Kaimoto, Kyzyl Monteiro, Mehrad Faridan, Jiatong Li, Samin Farajian, Yasuaki Kakehi, Ken Nakagaki, and Ryo Suzuki. 2022. Sketched reality: Sketching bi-directional interactions between virtual and physical worlds with ar and actuated tangible ui. In *Proceedings of the 35th Annual ACM Symposium on User Interface Software and Technology.* 1–12.

[38] Yuki Kakui, Kota Araki, Changyo Han, Shogo Fukushima, and Takeshi Naemura. 2022. Using a Dual-Camera Smartphone to Recognize Imperceptible 2D Barcodes Embedded in Videos. In *Adjunct Proceedings of the 35th Annual ACM Symposium on User Interface Software and Technology* (Bend, OR, USA) *(UIST '22 Adjunct).* Association for Computing Machinery, New York, NY, USA, Article 87, 3 pages. https://doi.org/10.1145/3526114.3558672

[39] Daehwa Kim, Robert Xiao, and Chris Harrison. 2025. PatternTrack: Multi-Device Tracking Using Infrared, Structured-Light Projections from Built-in LiDAR. In *Proceedings of the 2025 CHI Conference on Human Factors in Computing Systems (CHI '25).* Association for Computing Machinery, New York, NY, USA, Article 552, 14 pages. https://doi.org/10.1145/3706598.3713388

[40] Yang Kuang and Meiling Zhu. 2017. Design study of a mechanically plucked piezoelectric energy harvester using validated finite element modelling. *Sensors and Actuators A: Physical* 263 (2017), 510–520.

[41] Tzu-Sheng Kuo and Eric Rawn. 2020. Let It Rip! Using Velcro for Acoustic Labeling. In *Adjunct Proceedings of the 33rd Annual ACM Symposium on User Interface Software and Technology* (Virtual Event, USA) *(UIST '20 Adjunct)*. Association for Computing Machinery, New York, NY, USA, 28–30. https://doi.org/10.1145/3379350.3416175

[42] Jiangtao Li, Angli Liu, Guobin Shen, Liqun Li, Chao Sun, and Feng Zhao. 2015. Retro-VLC: Enabling battery-free duplex visible light communication for mobile and IoT applications. In *Proceedings of the 16th International Workshop on Mobile Computing Systems and Applications*. 21–26.

[43] Jingyu Li, Qingwen Yang, Kenuo Xu, Yang Zhang, and Chenren Xu. 2025. EchoSight: Streamlining Bidirectional Virtual-Physical Interaction with In-situ Optical Tethering. In *Proceedings of the 2025 CHI Conference on Human Factors in Computing Systems (CHI '25)* (Yokohama, Japan). ACM, to appear. https://doi.org/tobeassigned Presented in the AR Interaction session, April 30, 2025.

[44] Xin Li, Hong Tang, Guobiao Hu, Bao Zhao, and Junrui Liang. 2021. ViPSN-pluck: A transient-motion-powered motion detector. *IEEE Internet of Things Journal* 9, 5 (2021), 3372–3382.

[45] Yichen Li, Tianxing Li, Ruchir A Patel, Xing-Dong Yang, and Xia Zhou. 2018. Self-powered gesture recognition with ambient light. In *Proceedings of the 31st annual ACM symposium on user interface software and technology*. 595–608.

[46] Kevin Liang, Chi-Wai Chow, and Yang Liu. 2016. RGB visible light communication using mobile-phone camera and multi-input multi-output. *Optics express* 24, 9 (2016), 9383–9388.

[47] Xin Liu, Bo Han, Clement Zheng, and Ching Chiuan Yen. 2022. Tribo Tribe: Triboelectric Interaction Sensing with 3D Physical Interfaces. In *CHI Conference on Human Factors in Computing Systems Extended Abstracts*. 1–6.

[48] Yuchi Liu, Hamideh Khanbareh, Miah Abdul Halim, Andrew Feeney, Xiaosheng Zhang, Hadi Heidari, and Rami Ghannam. 2021. Piezoelectric energy harvesting for self-powered wearable upper limb applications. *Nano Select* 2, 8 (2021), 1459–1479.

[49] Qian Lu, Xiaoying Yang, Xue Wang, Jacob Sayono, Yang Zhang, and Jeeeun Kim. 2025. LumosX: 3D Printed Anisotropic Light-Transfer. In *Proceedings of the 2025 CHI Conference on Human Factors in Computing Systems*. 1–21.

[50] Hiroyuki Manabe, Wataru Yamada, and Hiroshi Inamura. 2014. Tag system with low-powered tag and depth sensing camera. In *Proceedings of the 27th Annual ACM Symposium on User Interface Software and Technology* (Honolulu, Hawaii, USA) *(UIST '14)*. Association for Computing Machinery, New York, NY, USA, 373–382. https://doi.org/10.1145/2642918.2647404

[51] Muhammad Sarmad Shahab Mir. 2024. RGB LED for Communication, Harvesting and Sensing in IoT Applications. *ACM Transactions on Sensor Networks* 20, 5 (2024), 1–23.

[52] Areeba Naqvi, Ahsan Ali, Wael A Altabey, and Sallam A Kouritem. 2022. Energy harvesting from fluid flow using piezoelectric materials: a review. *Energies* 15, 19 (2022), 7424.

[53] Elham Maghsoudi Nia, Noor Amila Wan Abdullah Zawawi, and Balbir Singh Mahinder Singh. 2017. A review of walking energy harvesting using piezoelectric materials. In *IOP Conference Series: Materials Science and Engineering*, Vol. 291. IOP Publishing, 012026.

[54] Makoto Ono, Buntarou Shizuki, and Jiro Tanaka. 2013. Touch & activate: adding interactivity to existing objects using active acoustic sensing. In *Proceedings of the 26th Annual ACM Symposium on User Interface Software and Technology* (St. Andrews, Scotland, United Kingdom) *(UIST '13)*. Association for Computing Machinery, New York, NY, USA, 31–40. https://doi.org/10.1145/2501988.2501989

[55] Joseph A Paradiso and Mark Feldmeier. 2001. A compact, wireless, self-powered pushbutton controller. In *International Conference on Ubiquitous Computing*. Springer, 299–304.

[56] Pit Pillatsch, Eric M Yeatman, and Andrew S Holmes. 2014. A piezoelectric frequency up-converting energy harvester with rotating proof mass for human body applications. *Sensors and Actuators A: Physical* 206 (2014), 178–185.

[57] Michele Pozzi and Meiling Zhu. 2011. Plucked piezoelectric bimorphs for knee-joint energy harvesting: modelling andexperimental validation. *Smart Materials and Structures* 20, 5 (2011), 055007.

[58] PUIaudio. 2025. AB1070B-LW100-R, PIEZO BENDER. https://puiaudio.com/product/benders/ab1070b-lw100-r Last accessed 16 March 2025.

[59] Kun Qian, Yumeng Lu, Zheng Yang, Kai Zhang, Kehong Huang, Xinjun Cai, Chenshu Wu, and Yunhao Liu. 2021. {AIRCODE}: Hidden {Screen-Camera} communication on an invisible and inaudible dual channel. In *18th USENIX Symposium on Networked Systems Design and Implementation (NSDI 21)*. 457–470.

[60] Christian Rendl, David Kim, Sean Fanello, Patrick Parzer, Christoph Rhemann, Jonathan Taylor, Martin Zirkl, Gregor Scheipl, Thomas Rothländer, Michael Haller, and Shahram Izadi. 2014. FlexSense: a transparent self-sensing deformable surface. In *Proceedings of the 27th Annual ACM Symposium on User Interface Software and Technology* (Honolulu, Hawaii, USA) *(UIST '14)*. Association for Computing Machinery, New York, NY, USA, 129–138. https://doi.org/10.1145/2642918.2647405

[61] José Gerardo Rocha, Luís M Goncalves, PF Rocha, Marco P Silva, and Senentxu Lanceros-Mendez. 2009. Energy harvesting from piezoelectric materials fully integrated in footwear. *IEEE transactions on industrial electronics* 57, 3 (2009), 813–819.

[62] Valkyrie Savage, Andrew Head, Björn Hartmann, Dan B. Goldman, Gautham Mysore, and Wilmot Li. 2015. Lamello: Passive Acoustic Sensing for Tangible Input Components. In *Proceedings of the 33rd Annual ACM Conference on Human Factors in Computing Systems* (Seoul, Republic of Korea) *(CHI '15)*. Association for Computing Machinery, New York, NY, USA, 1277–1280. https://doi.org/10.1145/2702123.2702207

[63] Danny Scott, Matthew Bringle, Imran Fahad, Gaddiel Morales, Azizul Zahid, and Sai Swaminathan. 2024. NeuroCamTags: Long-Range, Battery-free, Wireless Sensing with Neuromorphic Cameras. *Proceedings of the ACM on Interactive, Mobile, Wearable and Ubiquitous Technologies* 8, 3 (2024), 1–25.

[64] Nurettin Sezer and Muammer Koç. 2021. A comprehensive review on the state-of-the-art of piezoelectric energy harvesting. *Nano energy* 80 (2021), 105567.

[65] Sitong Shen, Wenbo Ding, and Chenshu Wu. 2024. Self-Powered Visible Light Communication for Batteryless IoT via Vibration Energy Harvesting. In *Proceedings of the 12th International Workshop on Energy Harvesting and Energy-Neutral Sensing Systems*. 1–7.

[66] Yilei Shi, Haimo Zhang, Jiashuo Cao, and Suranga Nanayakkara. 2020. VersaTouch: A Versatile Plug-and-Play System that Enables Touch Interactions on Everyday Passive Surfaces. In *Proceedings of the Augmented Humans International Conference* (Kaiserslautern, Germany) *(AHs '20)*. Association for Computing Machinery, New York, NY, USA, Article 26, 12 pages. https://doi.org/10.1145/3384657.3384778

[67] Jaemin Shin, Seungjoo Lee, Taesik Gong, Hyungjun Yoon, Hyunchul Roh, Andrea Bianchi, and Sung-Ju Lee. 2022. MyDJ: Sensing Food Intakes with an Attachable on Your Eyeglass Frame. In *Proceedings of the 2022 CHI Conference on Human Factors in Computing Systems* (New Orleans, LA, USA) *(CHI '22)*. Association for Computing Machinery, New York, NY, USA, Article 341, 17 pages. https://doi.org/10.1145/3491102.3502041

[68] Ryo Takahashi, Masaaki Fukumoto, Changyo Han, Takuya Sasatani, Yoshiaki Narusue, and Yoshihiro Kawahara. 2020. TelemetRing: A Batteryless and Wireless Ring-shaped Keyboard using Passive Inductive Telemetry. In *Proceedings of the 33rd Annual ACM Symposium on User Interface Software and Technology* (Virtual Event, USA) *(UIST '20)*. Association for Computing Machinery, New York, NY, USA, 1161–1168. https://doi.org/10.1145/3379337.3415854

[69] Md. Farhan Tasnim Oshim, Julian Killingback, Dave Follette, Huaishu Peng, and Tauhidur Rahman. 2020. MechanoBeat: Monitoring Interactions with Everyday Objects using 3D Printed Harmonic Oscillators and Ultra-Wideband Radar. In *Proceedings of the 33rd Annual ACM Symposium on User Interface Software and Technology* (Virtual Event, USA) *(UIST '20)*. Association for Computing Machinery, New York, NY, USA, 430–444. https://doi.org/10.1145/3379337.3415902

[70] Ambuj Varshney, Andreas Soleiman, Luca Mottola, and Thiemo Voigt. 2017. Battery-free Visible Light Sensing. In *Proceedings of the 4th ACM Workshop on Visible Light Communication Systems* (Snowbird, Utah, USA) *(VLCS '17)*. Association for Computing Machinery, New York, NY, USA, 3–8. https://doi.org/10.1145/3129881.3129890

[71] Anandghan Waghmare, Qiuyue Xue, Dingtian Zhang, Yuhui Zhao, Shivan Mittal, Nivedita Arora, Ceara Byrne, Thad Starner, and Gregory D Abowd. 2020. UbiquiTouch: Self Sustaining Ubiquitous Touch Interfaces. *Proc. ACM Interact. Mob. Wearable Ubiquitous Technol.* 4, 1, Article 27 (mar 2020), 22 pages. https://doi.org/10.1145/3380989

[72] Robert Xiao, Scott Hudson, and Chris Harrison. 2016. CapCam: Enabling Rapid, Ad-Hoc, Position-Tracked Interactions Between Devices. In *Proceedings of the 2016 ACM International Conference on Interactive Surfaces and Spaces* (Niagara Falls, Ontario, Canada) *(ISS '16)*. Association for Computing Machinery, New York, NY, USA, 169–178. https://doi.org/10.1145/2992154.2992182

[73] Robert Xiao, Greg Lew, James Marsanico, Divya Hariharan, Scott Hudson, and Chris Harrison. 2014. Toffee: enabling ad hoc, around-device interaction with acoustic time-of-arrival correlation. In *Proceedings of the 16th International Conference on Human-Computer Interaction with Mobile Devices & Services* (Toronto, ON, Canada) *(MobileHCI '14)*. Association for Computing Machinery, New York, NY, USA, 67–76. https://doi.org/10.1145/2628363.2628383

[74] Wentao Xie, Huangxun Chen, Jing Wei, Jin Zhang, and Qian Zhang. 2024. RimSense: Enabling Touch-based Interaction on Eyeglass Rim Using Piezoelectric Sensors. *Proc. ACM Interact. Mob. Wearable Ubiquitous Technol.* 7, 4, Article 191 (Jan. 2024), 24 pages. https://doi.org/10.1145/3631456

[75] Jackie (Junrui) Yang and James A. Landay. 2019. InfoLED: Augmenting LED Indicator Lights for Device Positioning and Communication. In *Proceedings of the 32nd Annual ACM Symposium on User Interface Software and Technology* (New Orleans, LA, USA) *(UIST '19)*. Association for Computing Machinery, New York, NY, USA, 175–187. https://doi.org/10.1145/3332165.3347954

[76] Xiaoying Yang, Jacob Sayono, Jess Xu, Jiahao Nick Li, Josiah Hester, and Yang Zhang. 2022. MiniKers: Interaction-Powered Smart Environment Automation. *Proceedings of the ACM on Interactive, Mobile, Wearable and Ubiquitous Technologies* 6, 3 (2022), 1–22.

[77] Xiaoying Yang and Yang Zhang. 2021. CubeSense: Wireless, Battery-Free Interactivity through Low-Cost Corner Reflector Mechanisms. In *Extended Abstracts*

of the 2021 CHI Conference on Human Factors in Computing Systems. 1–6.

[78] Yanbing Yang and Jun Luo. 2020. Composite Amplitude-Shift Keying for Effective LED-Camera VLC. *IEEE Transactions on Mobile Computing* 19, 3 (2020), 528–539. https://doi.org/10.1109/TMC.2019.2897101

[79] Yanbing Yang, Jiangtian Nie, and Jun Luo. 2017. Reflexcode: Coding with superposed reflection light for led-camera communication. In *Proceedings of the 23rd Annual International Conference on Mobile Computing and Networking*. 193–205.

[80] Zhigang Yin, Mohan Liyanage, Abdul-Rasheed Ottun, Souvik Paul, Agustin Zuniga, Petteri Nurmi, and Huber Flores. 2023. HIPPO: Pervasive Hand-Grip Estimation from Everyday Interactions. *Proc. ACM Interact. Mob. Wearable Ubiquitous Technol.* 6, 4, Article 209 (Jan. 2023), 30 pages. https://doi.org/10.1145/3570344

[81] switches ZF sensors and energy harvesting. 2024. Energy Harvesting Generators. https://switches-sensors.zf.com/us/product/energy-harvesting-generators/ Last accessed 22 March 2024.

[82] Dingtian Zhang, Jung Wook Park, Yang Zhang, Yuhui Zhao, Yiyang Wang, Yunzhi Li, Tanvi Bhagwat, Wen-Fang Chou, Xiaojia Jia, Bernard Kippelen, et al. 2020. OptoSense: Towards ubiquitous self-powered ambient light sensing surfaces. *Proceedings of the ACM on interactive, mobile, wearable and ubiquitous technologies* 4, 3 (2020), 1–27.

[83] Kai Zhang, Chenshu Wu, Chaofan Yang, Yi Zhao, Kehong Huang, Chunyi Peng, Yunhao Liu, and Zheng Yang. 2018. ChromaCode: A Fully Imperceptible Screen-Camera Communication System. In *Proceedings of the 24th Annual International Conference on Mobile Computing and Networking* (New Delhi, India) *(MobiCom '18)*. Association for Computing Machinery, New York, NY, USA, 575–590. https://doi.org/10.1145/3241539.3241543

[84] Peiyu Zhang, Wen Ying, Sara L Riggs, and Seongkook Heo. 2024. MoiréTag: A Low-Cost Tag for High-Precision Tangible Interactions without Active Components. *Proc. ACM Hum.-Comput. Interact.* 8, ISS, Article 525 (Oct. 2024), 19 pages. https://doi.org/10.1145/3698113

[85] Xiao Zhang, Jiqiang Liu, Zhongjie Ba, Yaodong Tao, and Xiaochun Cheng. 2022. MobiScan: An enhanced invisible screen-camera communication system for IoT applications. *Transactions on Emerging Telecommunications Technologies* 33, 4 (2022), e4151.

[86] Yang Zhang, Yasha Iravantchi, Haojian Jin, Swarun Kumar, and Chris Harrison. 2019. Sozu: Self-powered radio tags for building-scale activity sensing. In *Proceedings of the 32nd Annual ACM Symposium on User Interface Software and Technology*. 973–985.

[87] Clement Zheng, Peter Gyory, and Ellen Yi-Luen Do. 2020. Tangible interfaces with printed paper markers. In *Proceedings of the 2020 ACM designing interactive systems conference*. 909–923.

# A APPENDIX

## A.1 Circuit Diagram

Figure 17 and Figure 18 include full schematic of all circuits used in the paper.
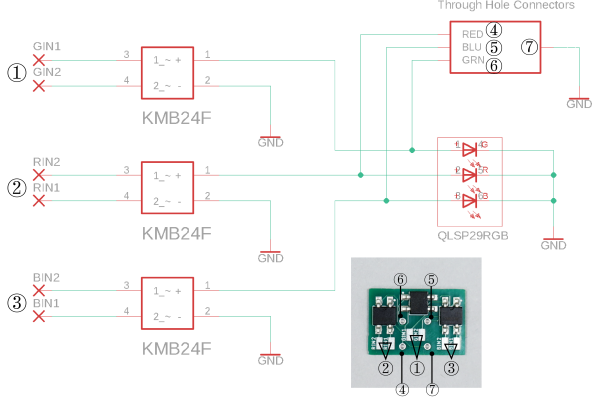


**Figure 17: Schematic of our circuit board. The numbers indicate the connection interface. ①, ② and ③ are to connect three piezos for three color channels. ④, ⑤, ⑥, ⑦ are through-holes for connecting resistive sensors.**
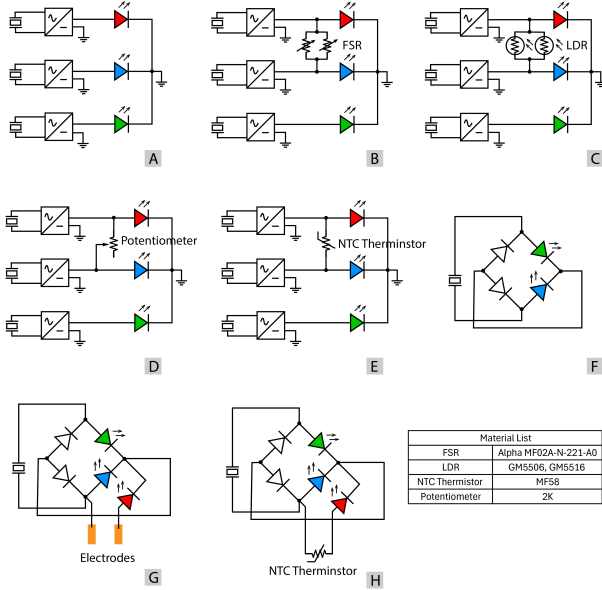


**Figure 18: Circuit diagrams for (A) hinge box, pill bottle, and zipper bag, (B) paper towel and water storage sensing, (C) trash can storage sensing, (D) knob interactors, (E) faucet temperature sensing, (F) push button, (G) conductivity and (H) temperature sensing for the finger probe.**
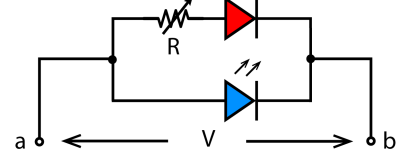
## A.2 LED Color Generation



**Figure 19: Red and blue LED branches.**

In our study, we used a tri-color LED, where the red, green, and blue LED branches can be controlled independently, and the resulting emitted color formed by the combined contributions of the three branches. The color of our "X" symbol embedded with sensing information is generated by the red and blue color channels with resistive sensors in the red LED branch. When $R = 0$, only the red LED turns on, clamping the voltage across the blue LED (i.e., $V_{ab}$) below its ON voltage ($V_{bo}$). This is because the current-driven and non-linear properties of LEDs, and the limited current supplied by our piezos (hundreds of $\mu A$) prevent the voltage $V_{ab}$ from increasing when the red LED conducts. When $R$ increases from 0 within a small range, $V_{ab} = IR + V_{red}$ increases until $V_{ab} = V_{bo}$ and the blue LED turns on. The voltage is subsequently clamped to $V_{bo}$, and current through the red LED branch $i_r = \frac{V_{bo} - V_{ro}}{R}$ decreases until it is completely off. Since the light intensity of LED relies on its forward current, the color gradually shifts from red to blue.

LEDs of different colors are typically manufactured with different luminous intensities (measured in mcd) even under the same power supply. Both the characteristics of the power sources, and the difference of ON voltage of the two LEDs, determine color responses to resistance changes.

This color-shifting phenomenon was observed using our piezo-electric energy harvesters as power sources, featuring high impedance and supplying limited power to the LEDs. For other power sources with different power characteristics, the the mapping between resistance and color may vary. For example, for power sources capable of supplying higher current, setting $R = 0$ allows allows the red LED branch to conduct more current, which can raise the voltage $V_{ab}$ enough to activate the blue LED branch as well. The overall color can be a combination of blue and red colors.

We leveraged the inherent difference in forward voltage in R, G, B LED (typically $\Delta V_f < 1V$, $V_{rf} < V_{gf} \approx V_{bf}$), which constrains the effective resistance $R$ to the range of tens to hundreds of kilo ohms based on the available current output of our plucking and striking mechanisms. We also find that by connecting a zener diode in series in one LED channel can shift the particular LED ON voltage to $V_o + V_z$ to adjust the operation points of each LED, thus adjusting the resistance range.